

A HIGH RESOLUTION STUDY OF THE ATOMIC HYDROGEN IN CO-RICH EARLY-TYPE GALAXIES

D. M. LUCERO^{1,2} AND L. M. YOUNG¹

Draft version June 16, 2021

ABSTRACT

We present an analysis of new and archival VLA HI observations of a sample of eleven early-type galaxies rich in CO, with detailed comparisons of CO and HI distributions and kinematics. The early-type sample consists of both lenticular and elliptical galaxies in a variety of environments. A range of morphologies and environments were selected in order to give a broader understanding of the origins, distribution, and fate of the cold gas in early-type galaxies. Six of the eleven galaxies in the sample are detected in both HI and CO. The H₂ to HI mass ratios for this sample range from 0.2-120. The HI morphologies of the sample are consistent with that of recent HI surveys of early-type galaxies which also find a mix of HI morphologies and masses, low HI peak surface densities, and a lack of HI in early-type galaxies which reside in high density environments. The HI-detected galaxies have a wide range of HI masses (1.4×10^6 to 1.1×10^{10} M_⊙). There does not appear to be any correlation between the HI mass and morphology (E versus S0). When HI is detected, it is centrally peaked - there are no central kpc-scale central HI depressions like those observed for early-type spiral galaxies at similar spatial resolutions and scales. A kinematic comparison between the HI and CO indicates that both cold gas components share the same origin. The primary goal of this and a series of future papers is to better understand the relationship between the atomic and molecular gas in early-type galaxies, and to compare the observed relationships with those of spiral galaxies where this relationship has been studied in depth.

Subject headings: atomic data — ISM: atoms — ISM: kinematics and dynamics — galaxies: elliptical and lenticular — galaxies: individual(NGC 83, UGC 1503, NGC 807, NGC 2320, NGC 3032, NGC 3656, NGC 4459, NGC 4476, NGC 4526, NGC 5666) — radio lines: ISM

1. INTRODUCTION

It is well known that many early-type galaxies (E and S0) contain significant amounts of cold gas (Wiklind et al. 1995; Young 2002; Welch & Sage 2003; Sage & Welch 2006; Morganti et al. 2006; Sage et al. 2007; Combes et al. 2007; Osterloo et al. 2007; di Serego Alighieri et al. 2007; Welch et al. 2010; Young et al. 2011). The evolutionary pathway of early-type galaxies is thought to be driven in part by the acquisition and transformation of this cold gas into new stars. To the best of our knowledge stars form only from the molecular gas phase. Clearly, knowledge of the amount of cold gas in the molecular phase versus the atomic phase is an important constraint for theoretical models of star formation and galaxy evolution.

Currently, the physical processes which determine the balance of the atomic and molecular gas are poorly understood in early-type galaxies. The question of molecule formation has been thoroughly studied in the literature mostly through two different methods. The first is an empirical study using the CO and HI maps of nearby disk galaxies (Blitz & Rosolowsky 2004, 2006; Leroy et al. 2008). These studies infer that the molecular to atomic surface density ratio in disks is entirely a function of the hydrostatic midplane pressure which is in turn a function of the stellar and gas volume densities (hereafter BR06 model). The second method also utilizes gas

maps and a first principles approach which models the chemical and physical processes that regulate the balance between the formation and dissociation of H₂ molecules (Elmegreen 1993; Krumholz et al. 2008, 2009; McKee & Krumholz 2010). Interestingly, both of these approaches predict values of the molecular fraction, $F_{mol} = \Sigma_{H_2} / \Sigma_g$, with $\Sigma_g = \Sigma_{H_2} + \Sigma_{HI}$, which are roughly consistent with molecular and atomic observations in nearby disk galaxies (Krumholz et al. 2009). Fumagalli et al. (2010) suggest that the two approaches yield similar values of the molecular fraction, because Blitz & Rosolowsky (2006) use a fixed stellar density typical of nearby disk galaxies and in effect both formalisms become a sole function of the total gas column density.

Testing whether photo-dissociation and star formation laws (empirical and theoretical) hold in early-type galaxies requires detailed information about the spatial distribution, column density, and kinematics of both the atomic and molecular gas components. There has been a recent explosion in the number of available HI and CO maps of early-type galaxies (e.g. Serra et al. 2012; di Serego et al. 2007; Osterloo et al. 2007; Alatalo et al. 2012). However, most of these HI maps have resolutions $\geq 45''$ and so are not at high enough resolution to make an adequate comparison with existing CO interferometric observations which typically have resolutions $\leq 7''$. In this paper we present the first comparison of high-resolution HI and CO observations in a sample of eleven early-type galaxies. The new HI observations have 2 to 16 times better resolution than the current HI surveys.

¹ Physics Department, New Mexico Institute of Mining and Technology, Socorro, NM 87801, USA

² Department of Astronomy, University of Cape Town, Rondebosch 7701, Republic of South Africa

Higher resolution observations of the HI can also help us to better constrain the origins of the cold gas. There are two basic models for the origin of the cold gas in early-type galaxies: internal and external. The internal origin means mass loss from the stars in the galaxy itself. Estimates of the stellar mass loss rate are certainly more than enough to reproduce the cold gas contents in early-types over a Hubble time (Faber & Gallagher 1976; Ciotti et al. 1991; Brighenti & Mathews 1997; Athey et al. 2002). However, recent observational studies of the cold gas in nearby early-type galaxies show that on average the total observed gas masses add up to only about 10% of what is expected from mass loss after the first 0.5 Gyr regardless of luminosity (e.g. Sage & Welch 2006; Welch et al. 2010). It has been speculated that most of the returned stellar mass is either quickly depleted in star formation, used to fuel a central AGN, stripped, or heated into an ionized phase. Possible external origins include gas accretion from mergers or accretion of primordial gas from the intergalactic medium (IGM).

A large amount of evidence is accumulating which suggests that the bulk of the cold gas in local early-type galaxies is likely supplied via external processes (e.g. Davis et al. 2011; Morganti et al. 2006; Serra et al. 2012; Emsellem et al. 2004; McDermid 2006a). Arguments for an external origin are supported by the fact that the cold gas mass in early-type galaxies only weakly correlate with other optical properties such as stellar luminosity and stellar velocity dispersion (e.g. Davis et al. 2011), the existence of tidal features in HI maps (Morganti et al. 2006; Serra et al. 2012), kinematic mismatch between cold gas and stars (Davis et al. 2011), and the existence of kinematically decoupled stellar cores (Emsellem et al. 2004; McDermid et al. 2006a). Some early-type galaxies do sometimes contain stellar discs which correlate with nuclear and global galaxy properties suggesting that the gas which formed these stars was produced via internal mass loss (Davis et al. 2011). However, in these cases it may be that galaxy wide processes in the most massive early-types or the early-types host environment are effectively destroying any signatures of an external origin (Davis et al. 2011).

Recent single dish observations of HI and CO in a volume limited ($\text{dec} \leq 10^\circ$, and distances < 20 Mpc) sample of early-type galaxies indicate that the atomic and molecular cold gas phases themselves could have separate origins (Welch & Sage 2003; Sage & Welch 2006; Sage et al. 2007; Welch et al. 2010). The key piece of evidence which support their hypothesis is that the HI and CO kinematics (line profiles) for many of their lenticular galaxies do not match. Sage & Welch (2006) speculate that the two cold gas phases in early-type galaxies are separate, because the molecular gas originates from stellar mass loss while the atomic gas has been acquired from an outside source (primordial or through mergers). This single dish survey compares HI data with angular resolutions $\geq 45''$ to CO data with angular resolutions of $55''$. A more recent ATLAS^{3D} volume limited multiwavelength survey of 260 early-type galaxies compares $45''$ resolution HI data to CO data with resolutions ranging from $3''$ to $10''$. Their data show that the ionized, atomic, and molecular gas in local early-type galaxies always have similar kinematics and so likely have a common origin (Davis et al. 2011; Alatalo et al. 2012). Resolving the

discrepancy between these two studies requires closely matched high resolution HI and CO data.

This is the first in a series of papers that aim to: (1) Use the cold gas kinematics and gas morphologies of our sample to look for indications of separate origins for the HI and CO in early-type galaxies. (2) Test theoretical models of star formation known for spiral galaxies. Is there evidence of star formation where star formation models predict it to occur? (3) Test whether the theoretical H_2 molecule formation models of Elmegreen (1993), Krumholz et al. (2008, 2009), McKee & Krumholz (2010) and the empirical models of Blitz & Rosolowsky (2004) can predict the observed molecular fraction in early-type galaxies.

In Paper 1 we present the results of the new HI observations. Paper I is organized as follows: In Section 2 the sample description is presented. In Section 3 we present the 21-cm HI observations and data reduction. In sections 4.1 and 4.3 we present the results of the observations, and the HI fluxes and masses. In section 5 we compare the HI and CO morphologies. In section 6 we present the HI kinematics and the dynamical masses. In section 7 we discuss the role of the environment on the HI morphology and the origin of the cold gas in early-type galaxies. In section 8 we present the conclusions.

2. SELECTION AND GALAXY PROPERTIES

Testing whether photo-dissociation and star formation laws (empirical and theoretical) hold in early-type galaxies requires detailed information about the spatial distribution, column density, and kinematics of both the atomic and molecular gas components. Recently it has been found that the most CO rich early-type galaxies are more likely to have high column density HI (Serra et al. 2012). Therefore, in order to maximize our chances of detecting and resolving HI we begin this preliminary study using a sample of early-types already known to be CO-rich. Our galaxy sample includes eleven of the fourteen galaxies recently mapped in $^{12}\text{CO} 1-0$ line with the Berkeley-Illinois-Maryland Association (BIMA) millimeter interferometer at Hat Creek, CA by Young (2002, 2005) and Young et al. (2008). The molecular gas in these eleven galaxies is located in very regular, symmetric rotating disks with diameters ranging from 0.7 to 12 kpc and they have H_2 masses in the range of 1.0×10^8 - $4.7 \times 10^9 M_\odot$ (Young 2002, 2005; Young et al. 2008).

All of the galaxies in our sample have an $r^{1/4}$ profile or a classification as E, E/SO or S0 in several catalogs. In some cases, these classifications are based on photographic evidence. In the case of NGC 5666, CCD imaging suggests that one of our sample galaxies may have a more complicated morphology (Donzelli & Davoust 2003).

Additionally, all of our early-type sample galaxies have estimates on the amount and location of star formation derived from high resolution radio continuum ($5''$), 24μ FIR, and UV maps which make them ideal objects for this preliminary study (Lucero & Young 2007; Young et al. 2009).

The sample galaxies have a wide variety of properties and environments. About half the galaxies are isolated, and the other half are located in loose groups or clusters (Virgo and Abell 569). Some have very smooth, regular morphologies, whereas others are classified as ‘‘peculiar’’ because of dust lanes, stellar shells and ripples, etc. The

TABLE 1
 Sample Galaxies

Galaxy	Type	RA (J2000.0)	DEC (J2000.0)	V_{helio} (km s ⁻¹)	D (Mpc)	M_K (mag)	Environ
N83	E0	00h21m22.4s	22d26m01s	6359 (27)	85.1(6.1)	-25.35	Group
U1503	E	02h01m19.8s	33d19m46s	5086(6)	71(5)	-23.69	field
N807	E	02h04m55.7s	28d59m15	4764(12)	66(5)	-24.74	field
N2320	E	07h05m42.0s	50d34m52s	5944 (15)	84(7)	-25.77	Abell 569
N3032	S0	09h52m08.2s	29d14m10s	1533(5)	21.2(1.9)	-21.98	field
N3656	IOpec	11h23m38.4s	53d50m31s	2869(13)	40(3)	-23.74	merg remn
N4150	S0	12h10m33.6s	30d24m06s	226(22)	13.7(1.6)	-21.70	Coma Group
N4476	SO ⁻	12h29m59.1s	12d20m55s	1978(12)	17.6(0.6)	-21.76	Virgo clust
N4526	S0	12h34m03.0s	07d41m57s	575(24)	17.3(1.5)	-24.71	Virgo clust
N4459	SO ⁺	12h29m00s	13d58m53s	1210(16)	16.1(0.4)	-23.88	Virgo clust
N5666	?	14h33m09.2s	10d30m39s	2221(6)	31(2)	-22.28	field

NOTE. — Environments and classifications are taken from (1)Young 2002, (2) Young et al. 2008 and (3) RC3. Distances are taken from (4) Young et al. 2009,

(5) NASA’s Extragalactic Database (NED) and (6) Lyon Extragalactic Database (LEDA).

Velocities are taken exclusively from NED; they refer to HI where available or to stellar

velocities. K-Band magnitudes are taken from integrated magnitudes in the 2MASS catalog (Skrutskie et al. 2006).

targets’ distances range up to 80 Mpc and optical luminosities are in the range $-25.80 \leq M_K \leq -21.7$. Thus, a study of these objects should give us a broad understanding of how the HI and CO are distributed in early-type galaxies.

The sample galaxies discussed in this paper have a similar range in K-band stellar luminosity and $M(\text{HI})/L_K$ as those in the ATLAS^{3D} survey. However, our sample is heavily biased towards objects with H₂ masses above $10^8 M_\odot$. Additionally about half of our galaxy sample reside at distances greater than 40 Mpc with a few a factor of two more distant. Table 1 contains ephemeris information for the galaxy sample.

One potential danger in making comparisons from single dish surveys is the large discrepancy of the fields of view between instruments used to observe HI and CO (e.g. 20'' for CO from the IRAM 30 meter, versus 3' for HI from the Arecibo 300 meter). However, for early-type galaxies at the distances of our sample, the evidence suggests there is little CO flux missing beyond the available fields of view. For example, Welch & Sage (2003) made multiple pointings on early-type galaxies with the 30m telescope but rarely found CO emission outside the central kpc. Consistent with that result, a recent comparison of the CO fluxes from the IRAM 30 meter and the Combined Array for Millimeter Wave Astronomy (CARMA) for a subsample of the ATLAS^{3D} early-type galaxies shows that the CO is often slightly more extended than the IRAM 30 meter primary beam (Alatalo et al. 2012), but a single pointing with the 30m usually recovers at least 50% of the total flux. Interferometric surveys carried out with the Berkley Maryland Illinois Array (BIMA) and CARMA find that the CO in early-type galaxies rarely extends outside their respective primary beams (e.g. Young 2002; Young et al. 2005; Alatalo et al. 2012).

3. OBSERVATIONS AND DATA REDUCTION

In order to test the current photo-dissociation and star formation models we require HI column density maps of the eleven early-type galaxies at angular resolutions comparable to what has already been obtained in CO. These column density maps will allow us to calculate

the surface density ratio Σ_{H_2}/Σ_{HI} as a function of radius. Therefore, new neutral hydrogen Very Large Array (VLA) observations were obtained for eight galaxies (NGC 83, UGC 1503, NGC 807, NGC 2320, NGC 3032, NGC 4526, NGC 4459, and NGC 4150). Five of these galaxies (NGC 83, UGC 1503, NGC 807, NGC 2320, and NGC 3032) were observed in the C configuration (projected baselines 0-15 k λ) between 1992 February and 2005 August. The VLA’s C configuration and its 15'' beam is the best compromise between sensitivity and resolution for the purpose of comparisons between the atomic and molecular gas in our sample galaxies, and is a factor of three better than recent HI surveys with the WSRT (e.g. Serra et al. 2012). NGC 4150, NGC 4459, and NGC 4526 were observed in the VLA D configuration (projected baselines 0-5 k λ) in 2005 December. These three galaxies were observed in the lower resolution D array because they were observed with single dish telescopes (NGC 4150: Arecibo 305 meter, NGC 4459 and NGC 4526: Effelsberg 100 meter; Huchtmeier & Richter 1986), but were not detected. The new VLA D configuration observations for these three galaxies are about a factor of 10 deeper than what was done at the single dish. Recent Westerbork Synthesis Radio Telescope (WSRT) HI observations for NGC 4150 produce a clear detection (Morganti et al. 2006). The WSRT data for NGC 4150 have a similar resolution to that of our new D array data (70'' \times 35''), velocity resolution (16 km s⁻¹), and an rms noise of 0.6 mJy beam⁻¹. VLA D configuration HI data for NGC 4476 were previously published by Lucero et al. (2005) and resulted in a non-detection. We obtained and re-reduced this data using similar techniques described in section 3.1 of Lucero et al. 2005 and were able to achieve a slightly better rms noise of 1 mJy beam⁻¹ in a primary beam corrected cube. We derive a new upper limit to the HI mass of $<6.7 \times 10^6 M_\odot$.

High-resolution ($\leq 15''$) VLA HI maps already exist for NGC 3656 and NGC 5666. We have obtained a high resolution HI image of NGC 3656 from Jacqueline van Gorkom which is originally published by Balcells et al. (2001). This image was made by combining VLA D, C, and B array data and yielded an HI mass of $2.0 \times 10^9 M_\odot$. High resolution HI data for NGC 4476 were previously

TABLE 2
Observation and Image Parameters

Galaxy	Config	Obs Dates	Program ID	Flux Cal	Velocity Range (km s ⁻¹)	TOS ^a (hrs)	Beam (")	Linear Resolution (kpc)	Channel (km s ⁻¹)	Noise (mJy beam ⁻¹)	N _{HI} Limit (10 ¹⁹ cm ⁻²)
N83	C	2005 Aug	AY159	0137+331	5900–6700	6.6	19.2×17.3	7.9×7.1	21	0.3	13
U1503	C	2002 Dec	AY135	0137+331	4800–5400	8.4	13.8×13.0	4.8×4.5	21	0.3	23
NGC807	D ^b	1985 Dec	AD174	3C48	4100–5400	16	48.5×44.2	15.5×14.1	42	0.5	13
	C	2002 Jul	AY135	0137+331	4100–5400	9.0	13.8×13.1	5.9×5.5	21	0.2	15
	C&D*	—	—	—	4100–5400	25	32.9×31.5	10.5×10.1	42	0.2	5.3
N2320	C	2005 Sep	AY159	0137+331	5200–6600	7.5	16.9×15.8	6.9×6.4	21	0.3	16
N3032 ^c	C	1992 Feb	AL263	0137+331	1228–1873	9.3	18.9×16.5	1.9×1.7	10	0.6	13
N3656 ^d	BCD	1996/7	AB819/791	1328+307	2365–3521	28	7.4×7.2	1.4×1.4	21	0.16	42
N4476	D	2002 Jan	AY128	1331+305	1637–2284	4	46.2×42.6	3.9×3.5	10.4	1.0	3.4
N4526	D	2005 Dec	AY161	1331+305	0–1300	1.1	64.0×50.5	5.4×4.2	21	0.7	3.0
N4459	D	2005 Dec	AY161	1331+305	600–1800	1.1	45.0×43.3	3.5×3.4	21	1.0	7.1
N4150	D	2005 Dec	AY161	1331+305	–100–600	1.1	54.5×52.0	3.6×3.5	21	1.0	4.9
N5666 ^e	AD	1986 Feb	AL111	3C286	1906–2533	4.8	55.0×44.7	8.3×6.7	21	0.4	2.3
	C	1986 Dec	AL111	3C286	1906–2533	13.3	16.0×14.5	2.4×2.2	21	0.5	36
	C&AD	—	—	—	1906–2533	18.1	35.9×31.7	5.4×4.8	21	0.7	6.1

NOTE. — *Combined C and D VLA configuration data. *A array transition into D array.

^aTOS is the total time on source galaxy in hours.

HI column density limits in this table are derived from a conservative 6σ of the rms noise in one channel.

References for archival data:

^bDressel 1987.

^cObserved by Ernest Sequist but not published.

^dBalcells et al. 2001

^eLake et al. 1987

published by Lucero et al. (2005) and resulted in a non-detection and an upper limit to the HI mass of $<6.7 \times 10^6 M_{\odot}$. We have re-reduced this data using similar techniques outlined in section 3.1 of Lucero et al. (2005) and were able to achieve a slightly lower rms noise of 1 mJy beam⁻¹ in a primary beam corrected cube. Four hours of VLA C array data for NGC 5666 were published by Lake et al. (1987), but no HI flux or mass is quoted in that paper. Additional time on NGC 5666 was obtained (~ 9 hrs in C array) but never published (Jacqueline van Gorkom in private communication). Analysis of the full 13 hours of VLA C array data for NGC 5666 is presented in this paper.

Table 2 gives specific dates, configurations, and time on-source for archive data as well as the new HI data. All data calibration and image formation was done using standard calibration tasks in the Astronomical Image Processing System (AIPS) package (Greisen 2003). Each galaxy was observed in one pointing centered roughly on the optical center of the galaxy. Phase drifts as a function of time are corrected by means of nearby point sources observed every 30 to 45 minutes. The absolute flux scale was set by observations of the sources 0137+331 or 1331+305 (whichever was closer to the galaxy in question). These two sources are also used to correct variations in the gain as a function of frequency (bandpass calibration). Comparisons of flux measurements on all the observed calibrators suggest that the absolute flux uncertainties are on the order of 10%. Variations in the bandpass are on the order of 1%. Initial imaging revealed which channel ranges were free of HI line emission. Continuum emission was subtracted directly from the raw uv data by making first-order fits to the line-free channels using the AIPS task UVLIN. For the cases where no line emission is visible in any of the channels, the line width of the CO is used to determine which channels should be free of HI emission. The calibrated data

are Fourier-transformed using several different uv data weighting schemes chosen to enhance the spatial resolution or the sensitivity to large-scale structures. Dirty images were cleaned down to a residual level of 1.0 times the rms noise fluctuations, and then primary beam corrected. Table 2 shows the velocity range covered and velocity resolution for each galaxy as well as the linear resolution (FWHM of the synthesized beam) and rms noise level in the final image cubes. Integrated intensity and mean velocity maps are made using the AIPS task MOMNT, as follows. The cleaned data cubes are smoothed in the velocity and spacial domains using Hanning and Gaussian functions, respectively. The width of the Hanning function used was typically 3 channels. The full width at half maximum (FWHM) of the Gaussian convolving kernel was typically 11 pixels. Smoothed cubes are then clipped at a level of 1σ and 2σ , respectively, defining a mask which is applied to the original cleaned cubes before integration over velocity.

The data reduction is straight forward in all cases except for the continuum subtraction for NGC 4459. The D array data for NGC 4459 are dominated by errors due to the bright continuum source associated with M87 ($\sim 1.6^{\circ}$ to the south of the phase center). The following methods were used to try and remove these errors. First we fit and subtracted the radio continuum using UVLIN on a cube whose phase center has been shifted to the position of M87. This produced a cube with an rms of ~ 0.7 mJy beam⁻¹, but with unstable baselines. The task UVLIN is known to leave residuals at the position of strong continuum sources resulting in unstable baselines. In order to minimize the residuals we next tried using the AIPS task UVSUB followed by UVLIN again shifting the phase center to the position on M87. UVSUB subtracts from the visibility data a Fourier sum of the clean components estimated by deconvolution of the continuum image. The use of UVSUB produced no improvement. We next subtracted the continuum in the image plane using

the AIPS task IMLIN. IMLIN fits a low order polynomial to the line free part of the spectrum of each pixel in an image cube (Cornwell et al. 1992). In this case the continuum model fit is derived from the line free channels using a first order polynomial. Both UVLIN and IMLIN have similar problems dealing with point sources that are far from the phase center. However, IMLIN may produce better results than UVLIN, because its errors scale with distance from the bright continuum source rather than from the phase center as they do when fitting with UVLIN. Indeed IMLIN was much more successful at removing the sidelobes of M87, but produced an rms noise 1.4 times larger than that of the previous two methods (~ 1 mJy beam $^{-1}$). HI upper limits in the following sections are derived from the IMLIN'd cube.

Lower resolution data for NGC 807 and NGC 5666 are reduced and combined with our new higher resolution data in order to maximize the sensitivity for the purpose of calculating as accurate a flux measurement as possible. The lower resolution data for NGC 807 and NGC 5666 consists of 16 hours in the VLA D array (Dressler 1987), and 5 hours in the VLA AD array (Lake et al. 1987), respectively. These two data sets were obtained from the VLA archive and reduced in a similar manner as described above through to continuum subtraction. For NGC 807 the continuum-subtracted C array data is smoothed to the velocity resolution of the lower resolution data using the VLA task SPECR. The lower resolution data is then shifted in frequency space using the AIPS task CVEL, which corrects topocentric to heliocentric velocities and resamples so that channel frequencies in the lower resolution data set correspond to the same channels as in the higher resolution data set. Next the high and low resolution frequency corrected data sets are combined together using the AIPS task DBCON and then imaged using similar methods as those described above. The two data sets are combined such that they contribute equally to the final cleaned image.

4. RESULTS

4.1. HI Non-Detections

No HI emission or absorption is visible in the data cubes for NGC 83, NGC 4476, and NGC 4526. Often the HI structures in early-type galaxies are much more extended than the CO emission, and in some cases a central HI hole may be present (Roberts & Haynes 1994; van Driel & van Woerden 1991; Serra et al. 2012). Therefore, two sets of primary beam corrected spectra were made for each of these galaxies. For both spectra we assume that the HI covers the same velocity range as the CO. The first spectrum is constructed by first using the CO maps to define a rectangular mask region within which "all" of the detected CO emission is located. In the case of NGC 83 and NGC 4526 all of the detected CO emission fits within the central HI beam and so only a single pixel spectrum is extracted. The intensity is then integrated over the same spatial region over the velocity range of the CO. The second spectrum is made in a similar manner except emission is summed over a square box with a side length approximately equal to the diameter D_{25} (de Vaucouleurs et al. 1991). These larger boxes are typically 10 times the size of the CO diameter and 2.3 to 5.5 times the effective radius as defined in Cappellari et al. (2011),

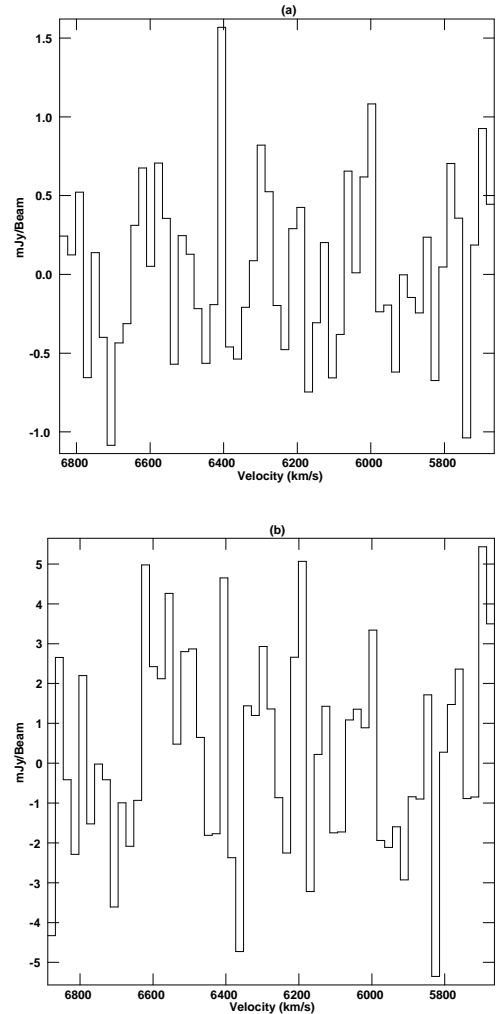


FIG. 1.— NGC 83: (a) HI spectrum of a square region, $5''$ on a side, centered on the optical center of NGC 83. The spectrum was constructed by first using the CO image to define a rectangular mask region within which the CO emission is located. The intensity was then integrated over the same spatial region for every channel, so the noise in the line free regions should be indicative of the noise on the line as well. (b) HI spectrum of a square region, $1.5''$ on a side, centered on the optical center of NGC 83. Integrated intensities quoted in the text are obtained from panel (a).

and they may reveal any extended, low surface brightness HI emission. The primary beam corrected HI spectra are depicted in Figures 1, 2, and 3. Spatial smoothing has not been employed, since the CO emission is smaller than the 15 beam of the C configuration for NGC 83 and the 45 beam of the D configuration for NGC 4526 and NGC 4476.

Upper limits to the HI fluxes for NGC 83, NGC 4476, and NGC 4526 are determined from the unresolved/CO like spectra (see Table 3). The uncertainty in the sum is calculated from the rms noise in the spectrum and the number of channels summed. This estimate assumes that the channels are uncorrelated. HI column densities and masses are obtained from three sigma upper limits of the uncertainty in the integrated intensity. Numerically, this mass limit (a 3σ limit on a sum over one beam and 20 to 30 channels) is within a factor of

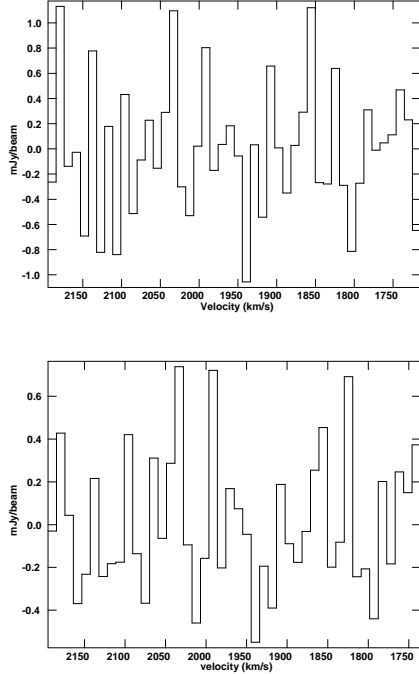


FIG. 2.— NGC 4476: As in Figure 1 but using box sizes of (t) $37''$ on a side, and (b) $1.1'$ on a side, centered on the optical center of NGC 4476.

two of that proposed by Serra et al. (2012), which is a 3σ limit on a sum over six beams and 40 km s^{-1} (1 to 4 of our channels). Thus, the mass limit we quote here is appropriate either for an HI distribution which is spatially compact and follows the CO emission in velocity, or for a modestly extended but narrow linewidth "cloud" of the type observed around some nearby early-type galaxies by Serra et al. (2012). HI column density and mass limits are obtained using "standard" formula, $N_{\text{HI}} = (1.1 \times 10^{24} \text{ cm}^{-2}) S_{\nu, \text{HI}} / (\theta_{\text{max}} \times \theta_{\text{min}})$ and $M(\text{HI}) = (2.36 \times 10^5 M_{\odot}) D^2 S_{\nu, \text{HI}}$, where $S_{\nu, \text{HI}}$ is the HI flux in units of Jy km s^{-1} , θ_{max} and θ_{min} are the major and minor axis of the synthesized beam in arcseconds, and D is the distance in Mpc. All derived parameters for the HI non-detections can be found in Table 3. No correction has been made for the presence of helium or effects due to inclination.

4.2. NGC 4459: A Tentative Detection?

For NGC 4459, spectra extracted from the central pixel (Fig. 4) appear to show low level HI emission. The IDL task GAUSSFIT is used to make a linear least square fit of a Gaussian to the spectrum in figure 4. The resulting fit produced a peak HI flux of $0.14 \pm 0.04 \text{ mJy}$, a full width at half maximum of $143 \pm 45 \text{ km s}^{-1}$ centered on $1307 \pm 19 \text{ km s}^{-1}$. The HI column density and HI mass derived from the fitted parameters are $1.1 \times 10^{20} \text{ cm}^{-2}$ and $1.2 \times 10^6 M_{\odot}$, respectively. The derived HI mass is consistent with a recent Westerbork Synthesis Telescope observation of similar resolution and slightly better rms noise ($0.64 \text{ mJy beam}^{-1}$) which produces an upper limit to the HI mass of $< 7.41 \times 10^6 M_{\odot}$ (Serra et al. 2012).

We regard this as a tentative detection for several reasons. First, The Gaussian fit is not in good agreement

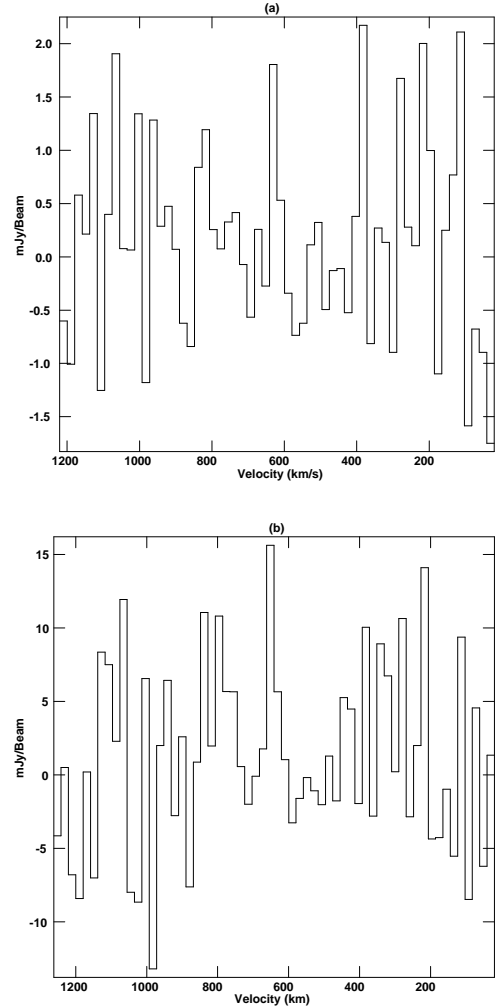


FIG. 3.— NGC 4526: As in Figure 1 but using box sizes of (a) $36''$ on a side and (b) $6.6'$ on a side, centered on the optical center of NGC 4526.

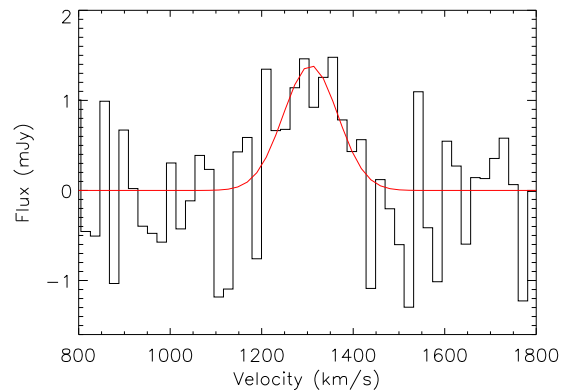


FIG. 4.— NGC 4459: HI spectrum for the central pixel ($15''$ on a side) centered on the optical center of NGC 4459. The CO in this galaxy fits inside the central pixel of the HI map. The red line is a Gaussian fit to the entire usable spectrum. The fit is centered on 1307 km s^{-1} , has an amplitude of 0.14 mJy , and a full width at half maximum, $\text{FWHM}/2.355 = 60.7 \text{ km s}^{-1}$.

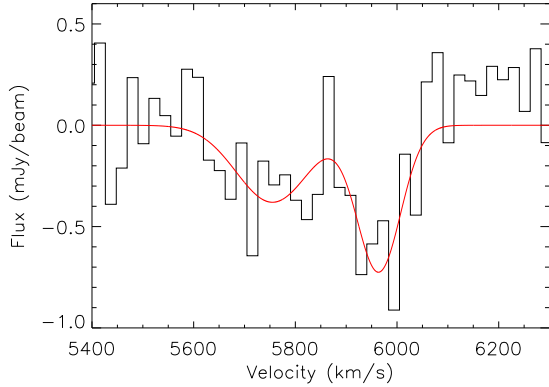


FIG. 5.— NGC 2320: HI spectrum extracted from one pixel across the entire usable velocity range (1197 km s^{-1}) centered on NGC 2320. The red line is a two component Gaussian fit to the entire usable spectrum. The narrow component is centered on 5964 km/s , has an amplitude of $-0.77 \text{ mJy beam}^{-1}$, and a full width at half maximum, $\text{FWHM}/2.355=101 \text{ km s}^{-1}$. The second component is centered on 5755 km s^{-1} , has an amplitude of $-0.38 \text{ mJy beam}^{-1}$, and a full width at half maximum, $\text{FWHM}/2.355=168 \text{ km s}^{-1}$.

with the CO observations which give a CO line width of 400 km s^{-1} centered on $1210 \pm 20 \text{ km s}^{-1}$ (Young et al. 2005) or with estimates of the systemic stellar velocities $1232 \pm 40 \text{ km s}^{-1}$ from Falco et al. (1999) and $1200 \pm 10 \text{ km s}^{-1}$ from Emsellem et al. (2004). Second, existing residual problems with the continuum subtraction produces spurious emission over large portions of the data cube (see section 3.1). HI column density and mass upper limits from our VLA data are also obtained using the methods described in section 4.1 (see Table 3).

4.3. HI Detections: Fluxes and Line Widths

4.3.1. HI Absorption

We detect no HI in emission for NGC 2320. There is HI emission present in the data cube for NGC 2320, but is associated with the spiral galaxy NGC 2321 (see appendix A). Despite the fact that the data cube for NGC 2320 still contains some residual side lobes from a nearby bright continuum source, the continuum flux is consistent with that of the value quoted in NRAO VLA Sky Survey ($19.3 \pm 0.7 \text{ mJy}$; Condon et al. 1998). Figure 5 shows a spectrum extracted from the pixel containing the radio continuum peak. This spectrum appears to show the presence of low level HI absorption. The absorption is asymmetric with a peak of $\sim -0.9 \pm 0.3 \text{ mJy beam}^{-1}$ centered near 6000 km s^{-1} and a weaker tail out to 5600 km s^{-1} . The absorption peak is only three times the rms noise, and the broader portion of the absorption is at or below noise level. Thus, we investigated the possibility that the absorption feature is just an instrumental effect by also inspecting continuum subtracted images of the phase and flux calibrators, but we find no similar central absorption features or other artifact associated with those cubes. There is an HI absorption artifact associated with a spiral galaxy, NGC 2321, that is located $10'$ from the phase center (see appendix section A.1). However, the channels which contain this artifact are offset by more than 100 km s^{-1} from the absorption feature associated with NGC 2320 and so both features are probably not due to an interference spike. We believe that the

absorption artifact in NGC 2321 is probably caused either by problems with the continuum subtraction and/or imaging of a source that is far from the phase center; in other words, it is not related to the feature in NGC 2320. It is also interesting to note here that the CO emission shows a small extension south west of the galaxy center, and the CO extension has similar velocities to the HI absorption peak ($6032\text{-}6282 \text{ km s}^{-1}$; See Figure 12 of Young 2005). This fact strengthens the possibility that at least the peak HI absorption is real. We proceed now with the assumption that the entire absorption is real.

We fit a two component Gaussian to the usable portion of the absorption spectrum in Figure 5. The narrow component has a peak intensity of $-0.72 \pm 0.17 \text{ mJy beam}^{-1}$ and a line width of $101 \pm 31 \text{ km s}^{-1}$ centered on $5964 \pm 13 \text{ km s}^{-1}$. The broader component has a peak intensity of $-0.38 \pm 0.14 \text{ mJy beam}^{-1}$ and a line width of $168 \pm 80 \text{ km s}^{-1}$ centered on $5755 \pm 31 \text{ km s}^{-1}$. The total velocity width of the two component fit is 425 km s^{-1} centered on 5862 km s^{-1} . The center velocity of the two component fit is in close agreement with both the systemic velocity of the CO ($5886 \pm 20 \text{ km s}^{-1}$; Young 2005) as well as measurements of the optical velocity ($5944 \pm 15 \text{ km s}^{-1}$; Smith et al. 2000 and $5725 \pm 60 \text{ km s}^{-1}$; de Vaucouleurs et al. 1991).

The optical depth calculated from the narrow and broad Gaussian fits are 0.043 ± 0.013 and 0.022 ± 0.007 , respectively. The estimated column density of the two components are $N_{HI} = 8.4 \pm 2.7 \times 10^{20} \text{ cm}^{-2}$ and $N_{HI} = 7.1 \pm 2.3 \times 10^{20} \text{ cm}^{-2}$, respectively. If both components represent real absorption the total column density is $N_{HI, \text{tot}} = 1.6 \pm 0.3 \times 10^{21} \text{ cm}^{-2}$. Alternatively, if the absorption is in actuality contained in just one channel the optical depth is 0.053 ± 0.010 , and the HI column density is $2.2 \pm 0.7 \times 10^{20} \text{ cm}^{-2}$ or $1.8 \pm 0.6 M_{\odot} \text{ pc}^{-2}$. The true HI column density probably falls somewhere between these three estimates. If the HI is smoothly distributed inside one beam ($\sim 42.7 \text{ kpc}^2$), the total HI mass and H_2/HI ratios range from $0.8\text{-}5.5 \times 10^8 M_{\odot}$ and 9 to 60, respectively. Both estimates of the HI mass and surface densities assume an HI harmonic mean spin temperature, $\langle T_s \rangle$, of $\sim 100 \text{ K}$ (Dickey & Lockman 1990) and are not corrected for the presence of helium.

4.3.2. HI Emission

For the galaxies with detected HI emission, Figures 7-18 show images of the integrated HI intensity, spectra, velocity fields, and individual channel maps. Total fluxes in Table 4 are measured from the integrated intensity images in the top panels of Figures 7-18. The uncertainties in the HI fluxes are about 10%, dominated mostly by the absolute calibration. HI column densities and masses are calculated using the fluxes listed in Table 4, distances from Table 1, and synthesized beams from Table 2. No correction has been made for the presence of helium or inclination effects.

A comparison of the new HI interferometric data with that of previous single dish observations yield the following: Our HI flux for NGC 807 is $10.3 \text{ Jy km s}^{-1}$ and is within 10% of the HI flux measured by Huchtmeier et al. (1995), hereafter HSH95, using the Effelsberg 100m telescope ($9.3'$ beam). Our HI flux for NGC 3032 is $0.64 \text{ Jy km s}^{-1}$ which is smaller than 0.9 Jy km s^{-1} measured

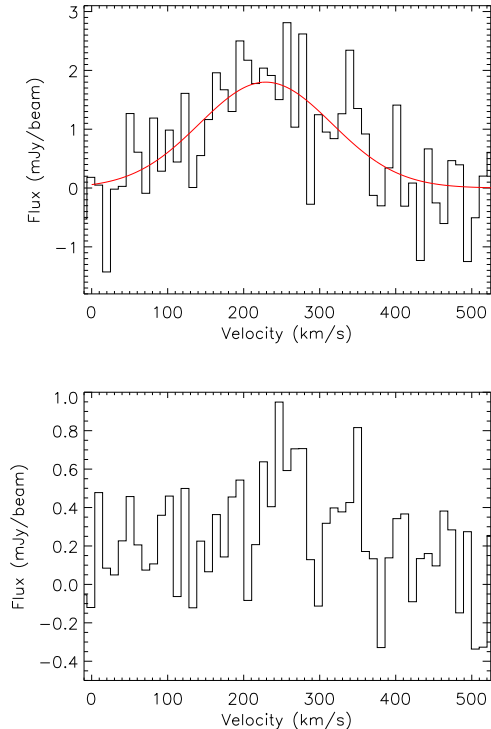


FIG. 6.— NGC 4150: As in Figure 1 but using box sizes of (a) $14''$ on a side and (b) $2.9''$ on a side, centered on the optical center of NGC 4150. Integrated intensities quoted in the text are obtained from panel (a). The red line in panel a is a Gaussian fit to the entire usable spectrum. The fit is centered on 229 km s^{-1} , has an amplitude of $1.8 \text{ mJy beam}^{-1}$, and a full width at half maximum, $\text{FWHM}/2.355=85.4 \text{ km s}^{-1}$.

with the Arecibo telescope and $0.96 \text{ Jy km s}^{-1}$ measured with the Westerbork at $45''$ resolution (Duprie & Schneider 1996; Serra et al. 2012). The Arecibo observations of NGC 3032 are three times less sensitive than our VLA C observations whereas the Westerbork observations are three times more sensitive. If the much lower sensitivity Arecibo observations detected all of the flux, and the lower resolution but higher sensitivity Westerbork observations detect all of the flux, then the VLA C array observations must be resolving out $\sim 30\%$ of the total HI flux. This is surprising in that the detected HI emission is so compact (i.e. there are probably no HI structures much larger than the primary beam). At about $10'$ to the northeast of NGC 3032 there are three distinct HI sources. A detailed presentation of the VLA HI observations for these three sources can be found in appendix A. HSH95 also detect a larger HI flux from UGC 1503, 3.3 Jy km s^{-1} , than is found for the VLA C array image (1.8 Jy km s^{-1}), but an earlier HI detection (1.7 Jy km s^{-1}) by Haynes & Giovanelli (1984) with the Arecibo telescope is consistent with the new observations. It is unclear whether HI emission from UGC 1503 has been missed by the VLA C array. The diameter of the HI emission in UGC 1503 is $\sim 1.5'$ so it is very unlikely that any emission could have been missed by the Arecibo observations. In the case of NGC 5666 the VLA C array observations recover a factor of 2 less flux than the VLA AD array ($3.8 \text{ mJy km s}^{-1}$ versus $6.2 \text{ mJy km s}^{-1}$). These two data sets have similar rms noises ($\sim 0.5 \text{ mJy beam}^{-1}$) and so it is likely that the C array observations have resolved

out a significant amount of flux. The HSH95 Effelsberg 100 meter single dish observations for NGC 5666 detect a smaller HI flux from NGC 5666, 4.5 Jy km s^{-1} , than is found for the combined VLA AD and C array image (6.3 Jy km s^{-1}). The rms noise of the HSH95 data, $\sim 1\text{--}2 \text{ mJy beam}^{-1}$, is about 2-4 times higher than the new observations. This is the most likely explanation for the smaller flux.

We find weak and poorly resolved HI emission in the data cube for NGC 4150 and spectra extracted from the central pixel appear to show low level HI emission (Fig. 6). Fitting a 1-D Gaussian to the spectrum in Figure 6a gives a full width at half maximum (FWHM) of $201 \pm 41 \text{ km s}^{-1}$ centered on $229 \pm 17 \text{ km s}^{-1}$ and a amplitude of $1.8 \pm 0.3 \text{ mJy beam}^{-1}$. The center velocity of the emission is in close agreement with both the systemic velocity of CO ($239 \pm 20 \text{ km s}^{-1}$; Young 2005) and measurements of the optical velocity ($226 \pm 22 \text{ km s}^{-1}$; Fisher et al. 1995). If the HI emission is unresolved the total flux is then $36 \pm 6 \text{ mJy km s}^{-1}$ which gives a total mass of $1.6 \pm 0.3 \times 10^6 M_{\odot}$. Similar WSRT observations yield an HI flux of 56 mJy km s^{-1} (Morganti et al. 2006). The WSRT observations have an angular resolution of $42.29'' \times 26.00''$. A total of four twelve hour tracks produced an rms noise of $0.3 \text{ mJy beam}^{-1}$, three times more sensitive than the VLA observations. The WSRT observations show that the HI in NGC 4150 is actually resolved (Morganti et al. 2006).

Recent single dish Arecibo HI observations of NGC 4150 by Sage & Welch (2006) produce spectra with similar line widths, but those authors quote an HI mass of $1.56 \times 10^7 M_{\odot}$ which is more than an order of magnitude larger than those derived from the interferometric data. One possible reason for the larger HI flux include is confusion with a nearby source. An analysis of the moment zero map (Fig. 15) provided by Raffaella Morganti shows that roughly half of the detected HI is located inside the galaxy ($\sim 1.4 \times 10^6 M_{\odot}$) while the other half is located outside of the galaxy ($\sim 1.6 \times 10^6 M_{\odot}$) about $1'$ to the south at a position of RA. 12h 10m 29.79s and Dec. 30d 22m 45.96s. The emission to the South does not appear to have any visible optical counterpart. In fact, there are no visible counter parts (in projection or velocity of $\pm 500 \text{ km s}^{-1}$) within $40'$ of NGC 4150 listed in the NASA Extragalactic database (NED). Therefore, it is unlikely that confusion with any additional field sources is occurring. A second possibility is confusion with high velocity galactic HI. This possibility can be ruled out since the high velocity clouds along the line of sight toward the position of NGC 4150 have negative velocities (Kalberla et al. 2005). A third possibility is that a significant amount of HI is in smooth, low density complexes that are only detected by the lower resolution instrument. This is the most plausible explanation since HI disks around early-types often extend significantly outside of their optical components (Sadler et al. 2000; Morganti et al. 2006; Grossi et al. 2009).

4.4. HI Column Densities and the $\frac{M_{\text{H}_2}}{M_{\text{HI}}}$ Mass Ratio

Our HI-detected sample galaxies have H_2/HI mass ratios ranging from 0.1 to 41 (see Table 4). This is a similar range in H_2/HI mass ratios found in both the single dish

TABLE 3
 HI Non-detections: Flux, Gas Masses, and Ratio Limits

Galaxy	Δ_{VCO}^a (km s ⁻¹)	I_ν^b (Jy km s ⁻¹)	S_ν^c (Jy km s ⁻¹)	N_{HI}^d (10 ²⁰ cm ⁻²)	M_{HI}^e (10 ⁷ M _⊙)	$\log\left[\frac{M_{HI}}{L_K}\right]$ ($\frac{M_\odot}{L_K}$)	M_{H_2} (10 ⁸ M _⊙)	$\frac{M_{H_2}}{M_{HI}}$	H ₂ ref
N83	6047-6464	0.043(0.030)	0.09	<3.0	<15	<-3.3	19(3)	>29	1
N4459	1029-1392	0.034(0.092)	0.28	<1.6	<1.7	<-3.6	1.7(0.3)	>21	2
N4476	1870-2050	0.12(0.03)	0.09	<12	<0.66	<-3.2	1.0(0.1)	>15	3
N4526	287-970	0.30(0.09)	0.27	<0.91	<1.9	<-3.9	6.4(1.5)	>100	2

NOTE. — No correction is made for the presence of helium or inclination effects in either the HI or the H₂ masses. H₂ mass references: (1) Young 2005; (2) Young et al. 2008; (3) Lucero et al. 2005.

^a The observed width of the CO line.

^b HI Intensity integrated over the CO line width.

^c Upper limit of the HI flux for an unresolved source derived from three times the uncertainty in the integrated intensity.

^d Estimated upper limit to the peak HI column density derived from S_ν .

^e Estimated upper limit to the HI Mass derived from S_ν .

 TABLE 4
 Detections: HI Fluxes, Gas Masses and Ratios

Galaxy	S_ν (Jy km s ⁻¹)	N_{HI} (10 ²⁰ cm ⁻²)	R_{HI} (arcsec)	R_{HI} (kpc)	M_{HI} (10 ⁸ M _⊙)	$\log\left[\frac{M_{HI}}{L_K}\right]$	M_{H_2} (10 ⁸ M _⊙)	$\frac{M_{H_2}}{M_{HI}}$	Class ^d	ref
U1503	1.8(0.2)	9.9	47	16(1)	21(3)	-1.47	19(3)	1	D	1
N807 ^a	10.3(0.9)	7.7	223	42(3)	110(15)	-1.17	14(3)	0.1	u/D	1
N2320 ^b	—	2.2-16.0	—	—	1.2-7.4	-2.75	47(9)	6-40	d	2
N3032	0.64(0.06)	13	24	2.5(0.3)	0.68(0.13)	-2.27	4.9(1.1)	7	d	3
N3656	5.4(0.5)	72	41	8.0(0.2)	20(3)	-1.51	38(5)	2	u	4
N4150	0.036(0.007)	0.49	—	—	0.016(0.004)	-3.79	0.58(1.1)	36	d	3
N4150 ^c	0.032(0.010)	0.29	45	3.0(0.3)	0.014(0.003)	-3.85	0.58(1.1)	41	d	5
N5666	6.3(0.6)	9.1	96	14(1)	14(2)	-1.08	4.4(0.6)	0.31	D	1

NOTE. — The value quoted in the third column is the observed peak HI column density. No correction is made for the presence of helium in either the HI or the H₂ masses.

^a The HI radius quoted for the disk of NGC 807 is measured from the galaxy center out to the edge or the tidal arms.

^b NGC 2320 is detected in absorption. The range in peak column density corresponds to the cases of narrow and broad absorption.

^c The HI flux and mass come from the WSRT observations. The quoted HI flux accounts for only the HI associated with the optical galaxy and excludes a patch of HI emission outside and $\sim 1'$ to the south of NGC 4150 (see section 4.3).

^d Morphological HI classifications as defined by the ATLAS^{3D} classification scheme (Serra et al. 2012).

References: (1) Young 2002; (2) Young 2005; (3) Young et al. 2008; (4) Balcells et al. 2001; (5) Morganti et al. 2006

and interferometric volume limited surveys. The single dish survey of Welch & Sage (2006) find H₂/HI mass ratios in the range of 0.01-5. The interferometric ATLAS^{3D} survey find H₂/HI mass ratios in the range of 0.01 to 36 (Serra et al. 2012). The lower end of the range in our mass ratio is an order of magnitude larger than that of the volume limited samples. This is probably due to the fact that our early-type sample is biased toward the most CO-rich objects. All of our sample galaxies with H₂/HI mass ratios greater than 10 reside in group or cluster environments. This is also consistent with what is found by the recent volume limited surveys. We discuss the role of environment on the HI content of our sample galaxies in section 7.1.

The interferometric observations for NGC 4150 give an $M_{H_2}/M_{HI} = 41$. However, this mass ratio may be too high since it is possible that the WSRT observations may have missed a significant amount of flux (see discussion in section 4.3.2). If the HI mass is instead derived from the Arecibo flux (Sage & Welch 2006) and the distance in Table 1, the mass ratio is much lower, $M_{H_2}/M_{HI} \sim 2$.

5. HI VERSUS CO MORPHOLOGY

The top panels of Figures 7, 10, 12, 14, 15, and 17 show integrated HI maps overlaid with each galaxy's respective molecular gas map. A wide-field image of the HI emission

for NGC 807 is depicted in the top panel of Figure 9. Figures 8, 11, 13, 16, and 18 show the individual channel maps. A detailed discussion of the HI morphology as compared to that of the CO is given for each galaxy below. Table 4 gives morphological classifications of the HI according to the ATLAS^{3D} classification scheme (Serra et al. 2012).

UGC 1503- This is an isolated early-type galaxy. The HI emission in this galaxy is detected over 288 ± 10 km s⁻¹ centered on a systemic velocity of 5086 ± 10 km s⁻¹. The HI systemic velocity is in good agreement with stellar absorption line velocity measurements of 5062 ± 43 km s⁻¹ from Falco et al. (1999) and 5098 ± 25 km s⁻¹ from Wegner et al. (2003). The HI systemic velocity is also in good agreement with the CO systemic velocity, 5080 ± 15 km s⁻¹, after correction from the radio to the optical definition (Young et al. 2002). The diameter of the HI emission is approximately $1.6'$. Like the CO emission, the HI in this galaxy is centrally peaked (0.16 Jy beam⁻¹ km s⁻¹ = 9.9×10^{20} cm⁻²) and centered on the optical center of the galaxy. An inspection of the integrated intensity map shows that HI is distributed into two concentric symmetric ring-like structures (Fig. 7). The central ring appears to be bisected by a bright bar like feature along the minor axis. Circular depressions

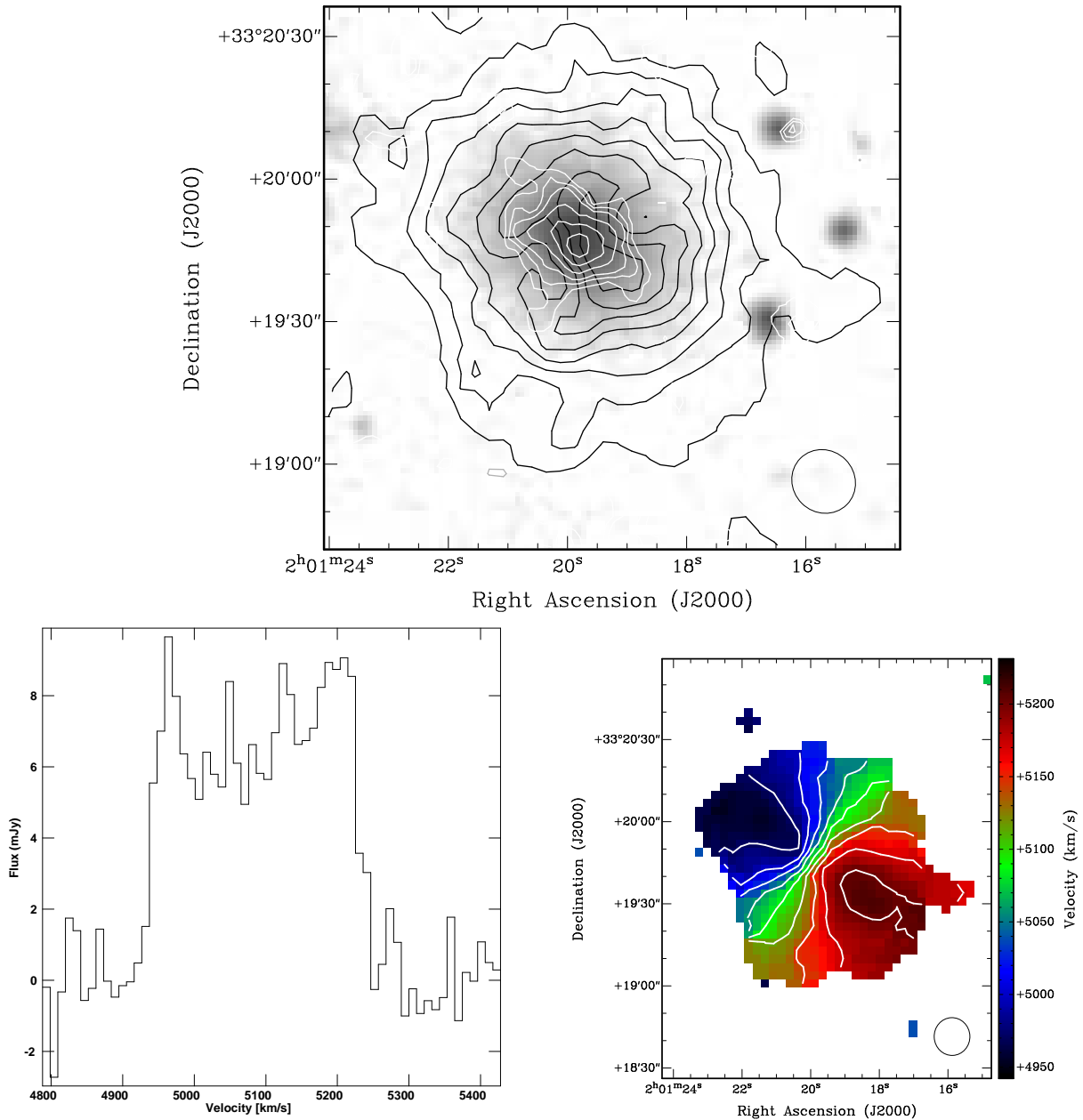


FIG. 7.— **Top:** UGC 1503: Solid black (positive) and grey (negative) contours show the HI integrated intensity in units of -10% , -20% , 10% , 20% , 30% , 40% , 50% , 60% , 70% , 80% , and 90% of the peak ($0.16 \text{ Jy beam}^{-1} \text{ km s}^{-1} = 9.9 \times 10^{20} \text{ cm}^{-2}$). White contours show the CO integrated intensity in units of 10% , 20% , 30% , 50% , 70% , and 90% of the peak ($6.3 \text{ Jy beam}^{-1} \text{ km s}^{-1} = 3.9 \times 10^{21} \text{ cm}^{-2}$). The grey scale image is an SDSS2 R-band image. **Bottom left:** HI spectrum. The spectrum was constructed by first using the integrated image (moment 0) to define a rectangular mask region within which the emission is located. The intensity was then integrated over the same spatial region for every channel, so that the noise in the line free channels is indicative of the noise on the line as well. **Right bottom:** Velocity field. The HI intensity-weighted mean velocity (moment 1) is shown in RGB color scale and in white contours from 4900 to 5200 km s^{-1} in steps of 30 km s^{-1} . The black ellipse shows HI the beam size. The CO resolution is $7.1'' \times 6.3''$.

or holes are observed symmetrically oriented inside the inner ring and about the central bar like feature. The highest surface densities are found in the bisecting bar like structure. The inner ring like structure lies at a radius of $12''$ and has a fairly constant surface density of $\sim 85 \text{ mJy beam}^{-1} \text{ km s}^{-1} = 5.2 \times 10^{20} \text{ cm}^{-2}$. The outer ring like structure is located at a radius of $24''$ and has a steadily declining surface density out to its edge. Both ring like structures are about one beam width in diameter and so are unresolved. It is interesting to note that the molecular gas does not appear to extend outside the

inner edge of the inner ring.

NGC 807- The HI in this galaxy is detected over 468 km s^{-1} centered on a systemic velocity of $4750 \pm 21 \text{ km s}^{-1}$. The HI systemic velocity is in good agreement with stellar absorption line velocity measurements of $4747 \pm 41 \text{ km s}^{-1}$ from Falco et al. (2000) and $4721 \pm 30 \text{ km s}^{-1}$ from Wegner et al. (2003). The HI systemic velocity is also in good agreement with the CO systemic velocity, $4728 \pm 25 \text{ km s}^{-1}$, after correction from the radio to the optical definition (Young et al. 2002). The lower resolution map made from the combined AD and C array data gives the

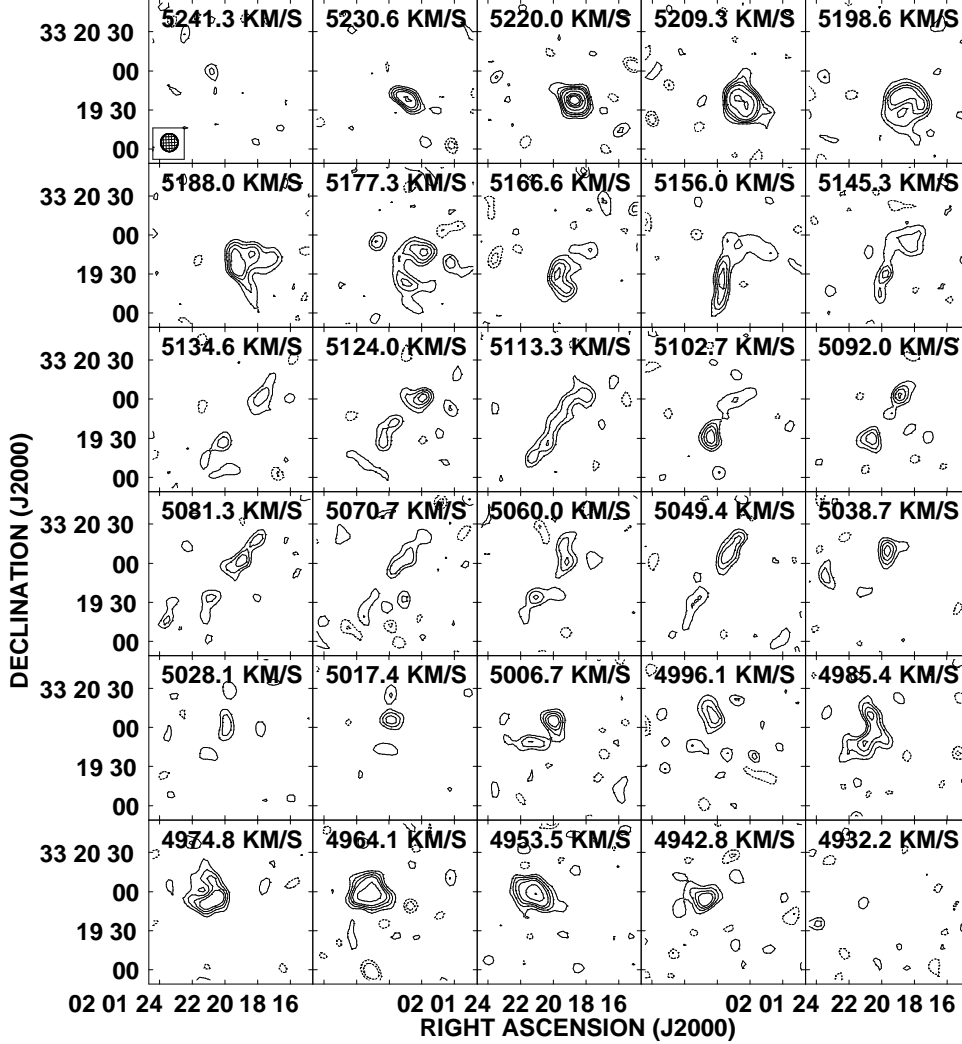


FIG. 8.— UGC 1503. Individual channel maps showing HI emission. Contour levels are $-3, -2, 2, 3, 4, 5, 7, 9, 10,$ and 11 times $0.3 \text{ mJy beam}^{-1} \sim 1\sigma$. The velocity of each channel (in km s^{-1}) is indicated at the top of each panel and the beam size in the first panel in the bottom left corner.

appearance of a smooth central HI disk with two tidal arms extending to the north west and south east along the major axis. The higher resolution C array data shows that the HI distribution is actually very clumpy and complicated (see the top panel of Figure 9). The HI in this galaxy is distributed about equally between the inner disk and the outer tidal arms with $\sim 5.5 \times 10^9 M_{\odot}$ in each component. The diameter of the HI emission out to the edge of the tidal arms is approximately $7.4'$. The inner disk has a radius of $\sim 2.7'$ and appears to be distributed asymmetrically with about 60% of the HI located to the northwest. The opposite is true of the tidal arms. The bulk of the HI in the tidal arms, $\sim 70\%$, is located in the arm to the southeast. The HI intensity is centrally peaked ($0.72 \text{ Jy beam}^{-1} \text{ km s}^{-1} = 7.7 \times 10^{20} \text{ cm}^{-2}$) and is roughly coincident with the CO intensity peak. However, the intensity peaks are slightly offset ($\sim 5-9''$) from the optical center of the galaxy. Interestingly, the CO distribution is also asymmetric, but the bulk of the CO emission ($\sim 70\%$) is actually located to the southeast.

NGC 2320- NGC 2320 is a member of the Abell 569 cluster of galaxies. The HI in this galaxy is detected only

in absorption. The absorption may be due to a small disk of HI which may not be large enough to be seen in emission due to the presence of the 17 mJy continuum source. There is a small extension of CO emission south west of the galaxy center which also has roughly the same velocity as the HI absorption peak ($6032-6282 \text{ km s}^{-1}$; See Figure 12 of Young 2005). This indicates that the absorbing HI and the CO extension could be part of the same gas complex which is actively falling in toward the center of the galaxy.

NGC 3032- NGC 3032 is a low luminosity field lenticular with a small counter rotating stellar disk of radius of $\sim 2''$ at its center (McDermid et al. 2006a). The HI in this galaxy is detected over 146 km s^{-1} centered on a systemic velocity of $1550 \pm 5 \text{ km s}^{-1}$, so the HI systemic velocity is in good agreement with the CO systemic velocity (Young et al. 2009) as well as with stellar absorption line velocity measurements of $1555 \pm 41 \text{ km s}^{-1}$ from Falco et al. (2004) and $1559 \pm 10 \text{ km s}^{-1}$ from Emsellem et al. (2004). The CO and HI line widths also match well. The C array data gives the appearance of a smooth HI disk. It is

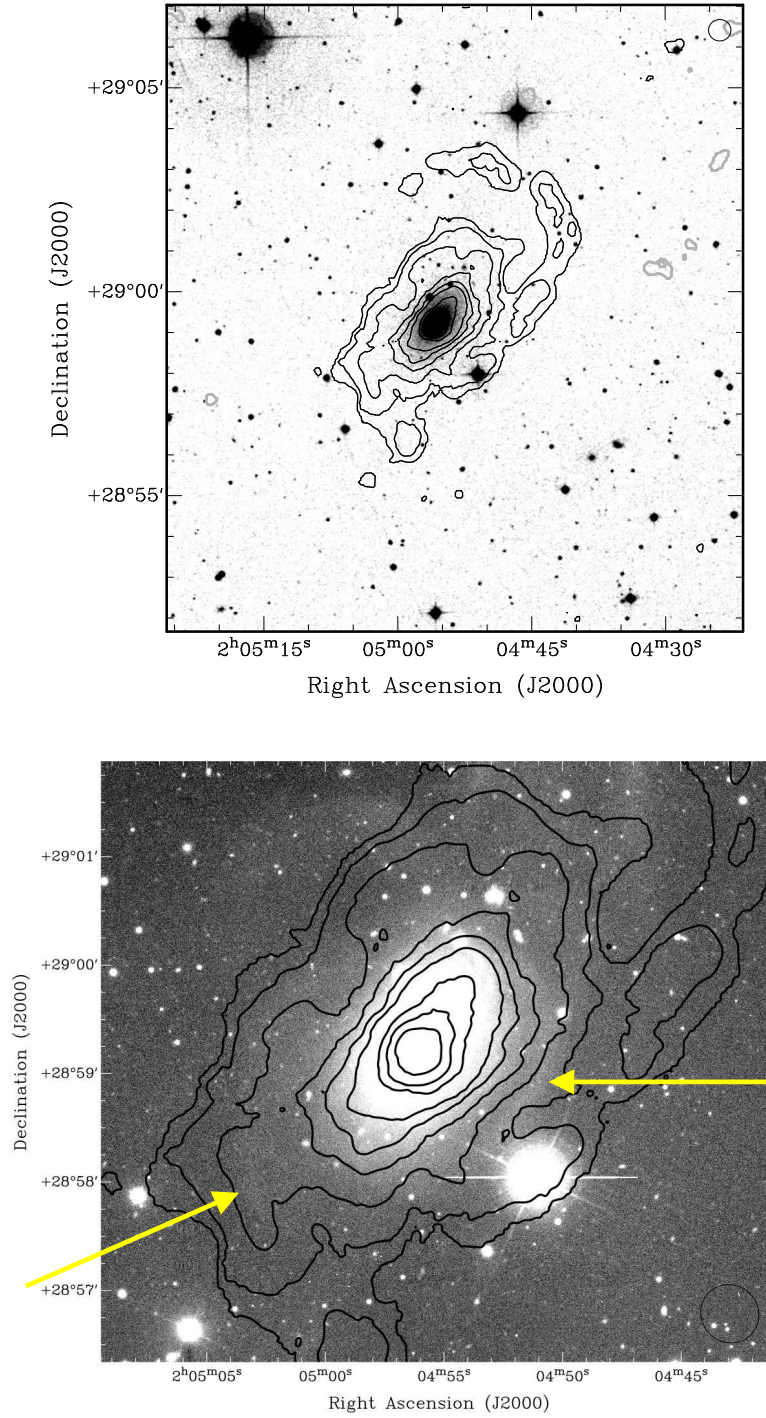


FIG. 9.— **Top:** NGC 807: VLA C+D array HI Data. Solid black (positive) and grey (negative) contours show the HI integrated intensity in units of -10%, -5%, 5%, 10%, 20%, 30%, 40%, 50%, 70%, 80%, and 90% of the peak ($0.72 \text{ Jy beam}^{-1} \text{ km s}^{-1} = 7.7 \times 10^{20} \text{ cm}^{-2}$). The black ellipse shows the beam size. The grey scale image is an SDSS2 R-band image. **Bottom:** HI contours overlaid on a WIYN 3.5 meter V band image. The black ellipse shows the beam size. Yellow arrows point to optical tidal features.

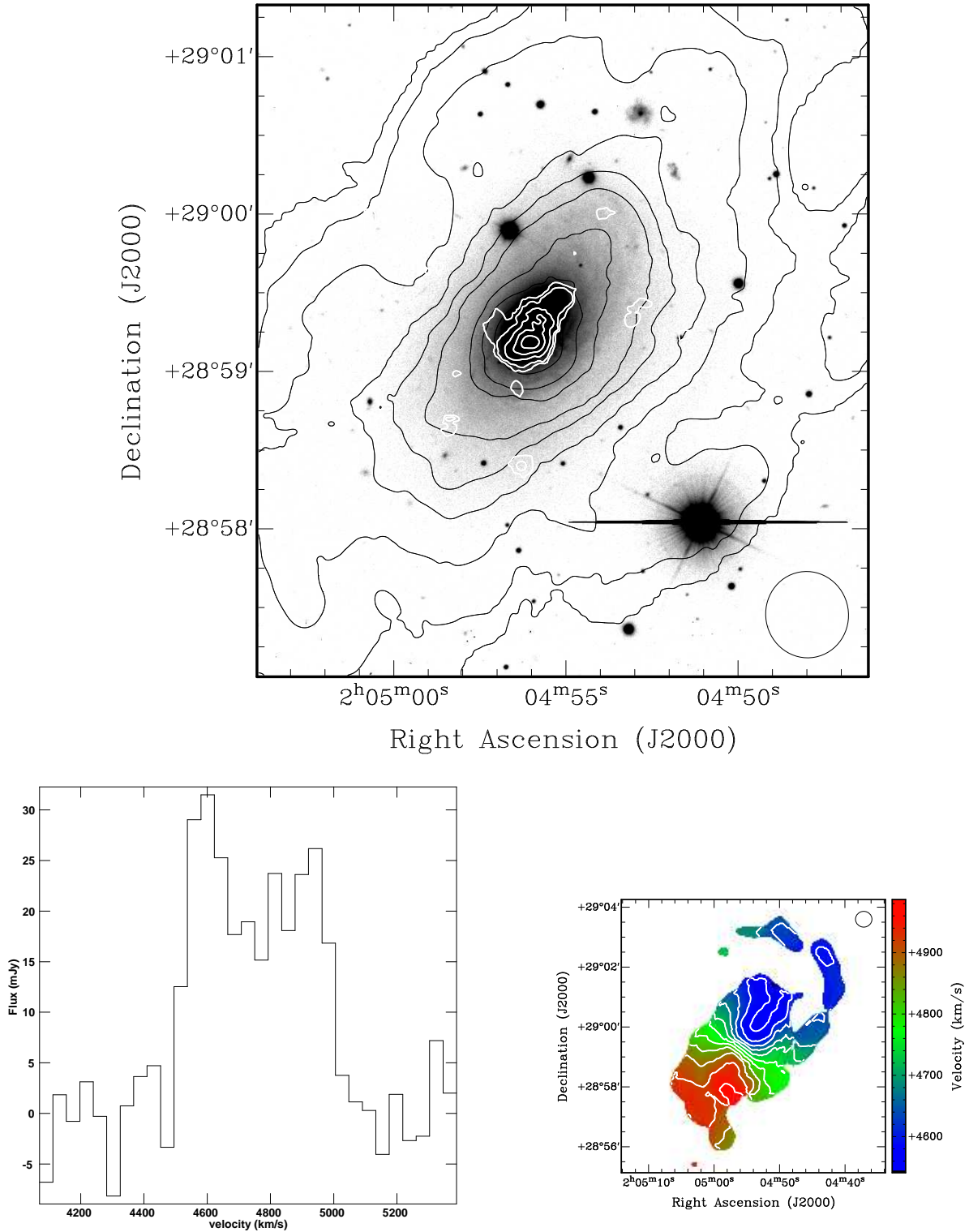


FIG. 10.— **Top:** NGC 807 zoomed in C+D array HI data overlaid with CO. Solid black (positive) and grey (negative) contours show the HI integrated intensity in units of -10%, -5%, 5%, 10%, 20%, 30%, 40%, 50%, 70%, 80%, and 90% of the peak ($0.72 \text{ Jy beam}^{-1} \text{ km s}^{-1} = 7.7 \times 10^{20} \text{ cm}^{-2}$). The black ellipse shows the beam size. white contours show the CO integrated intensity in units of 20%, 30%, 50%, 70%, and 90% of the peak ($7.6 \text{ Jy beam}^{-1} \text{ km s}^{-1} = 2.6 \times 10^{21} \text{ cm}^{-2}$). The grey scale image is an WIYN 3.5 meter V band image. **Left bottom:** HI spectrum. Constructed in a similar manner to UGC 1503. **Right bottom:** Velocity Field. The HI intensity weighted mean velocity (moment 1) is shown in RGB color scale and in white contours from 4560 to 4960 in steps of 40 km s^{-1} . The black ellipse shows the HI beam size. The CO resolution is $7.0'' \times 6.3''$.

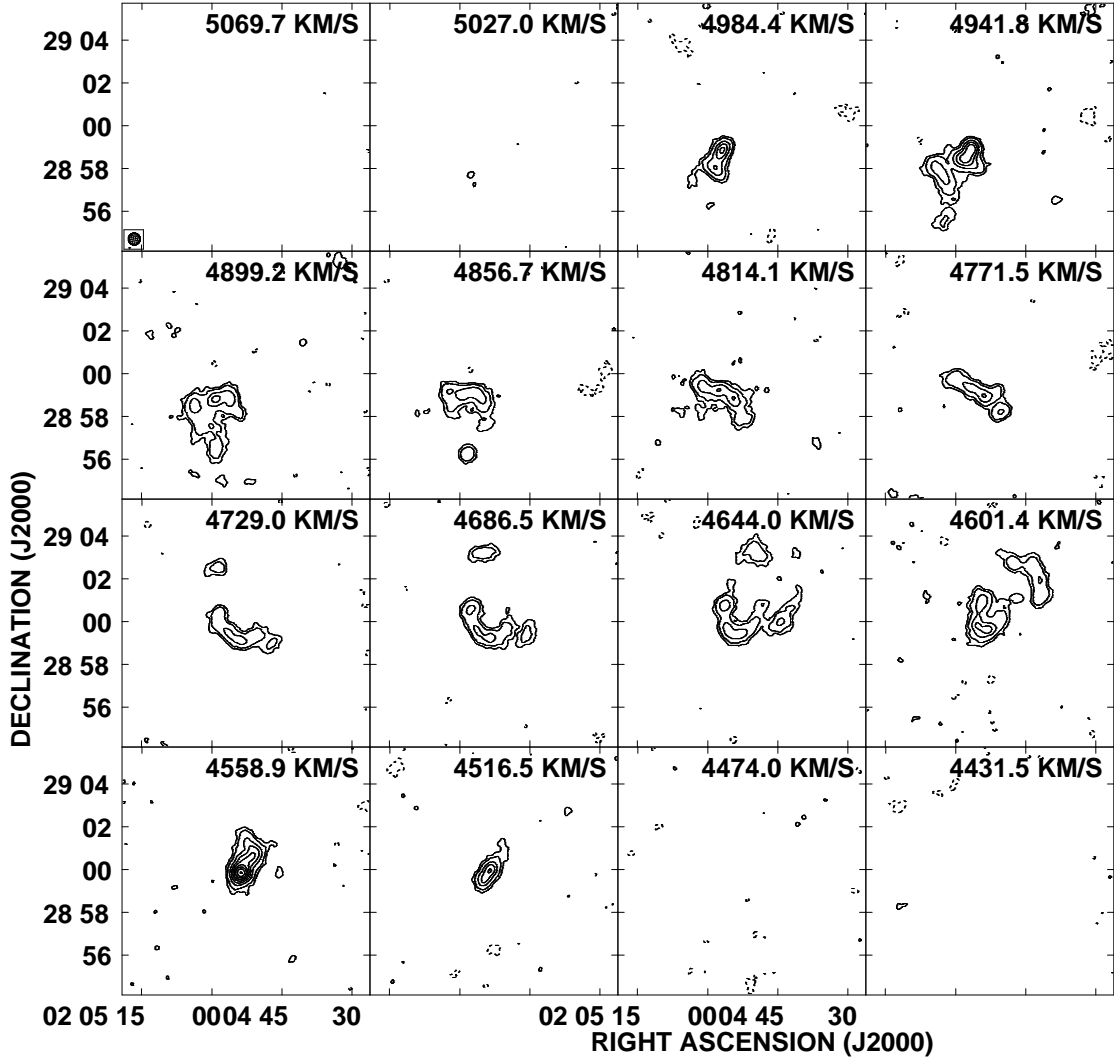


FIG. 11.— NGC 807: Individual channel maps showing HI emission. Contour levels are -5 , -3 , 3 , 10 , 15 , 20 , 25 , 30 , 35 , and 40 times 0.2 mJy beam $^{-1} \sim 1\sigma$. The velocity of each channel (in km s $^{-1}$) is indicated at the top of each panel and the beam size in the first panel in the bottom left corner.

apparent from the individual channel maps that the HI structures are not well resolved. The diameter of the HI emission is approximately $1'$ thus it is only slightly more extended than the CO emission. There is an extension of the HI gas ($\sim 6.8 \times 10^6 M_{\odot}$, roughly 10% of the total mass) outside the main disk to the south. This small amount of HI is oriented in roughly the same direction as a similar extension of the CO. The HI intensity is centrally peaked (0.38 Jy beam $^{-1}$ km s $^{-1} = 1.3 \times 10^{21}$ cm $^{-2}$) and roughly coincident with the optical and CO emission peaks.

NGC 3656- The HI data published by Balcells et al. (2001) shows that the HI in NGC 3656 is located in a nearly edge-on, warped minor-axis gaseous disk 7 kpc in diameter. The rest is situated outside the galaxy in what appear to be two tidal tails or perhaps a disrupted outer HI disk or ring. Balcells et al. (2001) note that the velocity structure of the HI distribution is asymmetric, indicating non-circular motions, and they suggest that this is due to recent or ongoing accretion. Their derived position angle of the inner HI disk is 170° and closely

matches the position angle derived from the Young's (2002) CO data. Balcells et al. (2001) HI systemic velocity of 2850 ± 11 km s $^{-1}$ is in good agreement with the CO systemic velocity of 2840 ± 15 km s $^{-1}$ (Young 2002) as well as with a stellar absorption line velocity measurement of 2890 ± 11 km s $^{-1}$ from Rothberg & Joseph (2006). The CO and HI line widths also match well. The HI intensity is centrally peaked (0.32 Jy beam $^{-1}$ km s $^{-1} = 6.6 \times 10^{21}$ cm $^{-2}$) and roughly coincident with the optical and CO emission peaks.

NGC 4150- NGC 4150 is a small nearby lenticular galaxy located on the outskirts of the Virgo Cluster at a projected distance of 18 degrees from M87 (Karachentsev et al. 2003). Morganti et al. (2006) quote an WSRT HI mass of $2.5 \times 10^6 M_{\odot}$, and describe the morphology of the HI inside the galaxy as that of a rotating disk with a diameter of about $1'$. A close inspection of the integrated intensity map reveals that the HI distribution in the disk is highly asymmetric. The bulk of the HI ($\sim 60\%$) is located in the Northwest portion of the stellar disk. The HI peaks at the center (30.4 mJy beam $^{-1}$

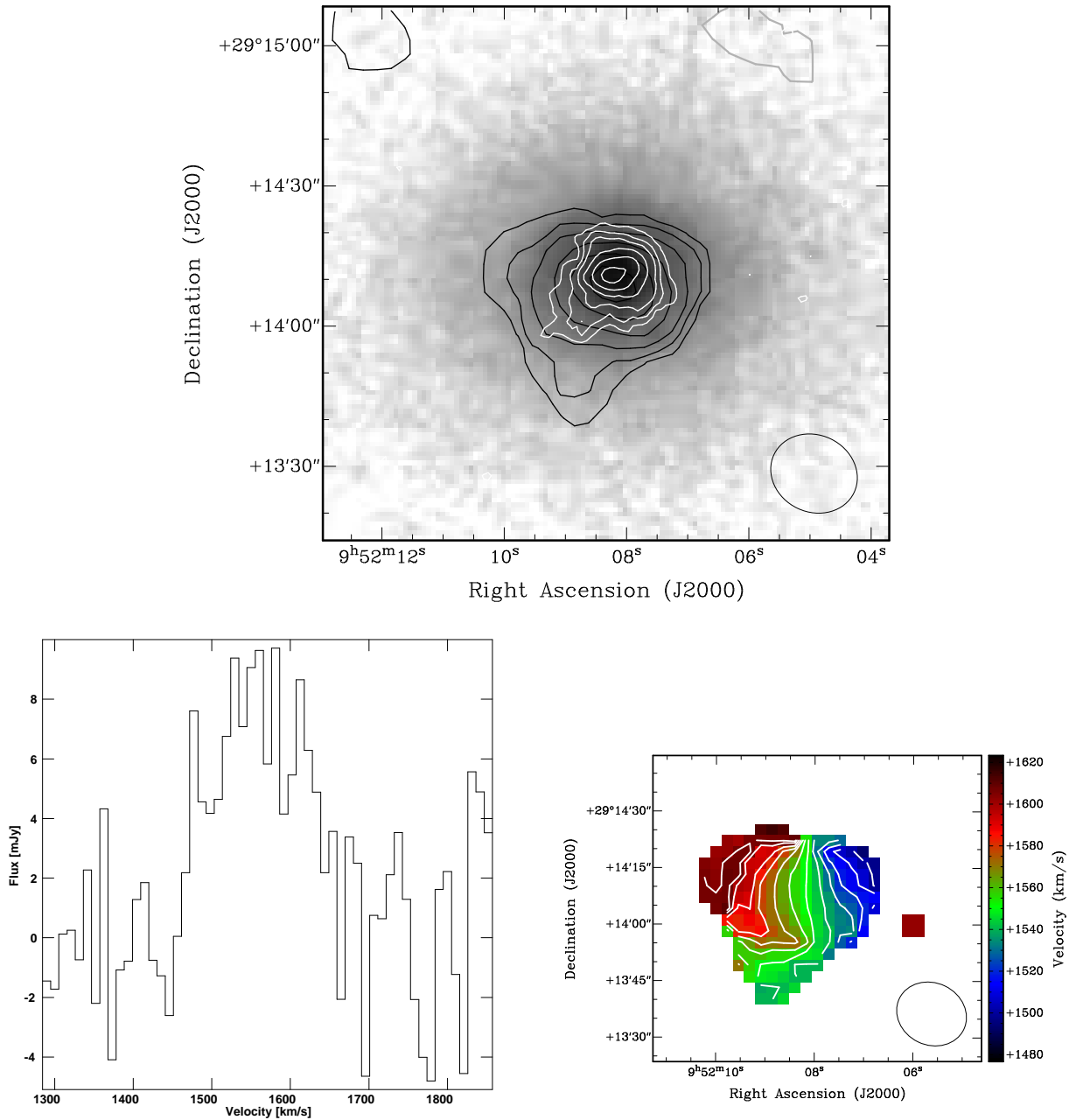


FIG. 12.— **Top:** NGC 3032: Solid black (positive) and grey (negative) contours show the HI integrated intensity in units of -5%, -15%, 5%, 15%, 30%, 50%, 70%, and 90% of the peak ($0.38 \text{ Jy beam}^{-1} \text{ km s}^{-1} = 1.3 \times 10^{21} \text{ cm}^2$). The ellipse shows the beam size. Green contours show the CO integrated intensity in units of -20%, -10%, 10%, 20%, 30%, 50%, 70%, and 90% of the peak ($18.1 \text{ Jy beam}^{-1} \text{ km s}^{-1} = 1.6 \times 10^{22} \text{ cm}^2$). **Left bottom:** HI spectrum. Constructed in a similar manner to UGC 1503. **Right bottom:** Velocity Field. The HI intensity-weighted mean velocity (moment 1) is shown in RGB color scale and in white contours from 1500 to 1610 km s^{-1} in steps of 10 km s^{-1} . The black ellipse shows the HI beam size. The CO resolution is $6.1'' \times 5.0''$.

$\text{km s}^{-1} = 3.04 \times 10^{19} \text{ cm}^{-2}$) and again at a radius of $17''$ along the major axis to the Northwest. There is a small unresolved clump of HI at the center of the disk that appears to be spatially coincident with the CO disk. The HI gas in the southern part of the disk has column densities up to 5 times lower than those in the northern and central components. The low surface density of the gas and the asymmetric distribution of the HI imply that the gas is currently being accreted from an outside source. Single dish observations show that the HI and CO have matching line width (Welch & Sage 2003).

NGC 5666- This is an isolated, low-luminosity field early-type galaxy. The HI emission in this galaxy is detected over $210 \pm 11 \text{ km s}^{-1}$ centered on a systemic velocity of $2219 \pm 10 \text{ km s}^{-1}$. The HI systemic velocity is in good agreement with stellar absorption line velocity measurements of $2222 \pm 40 \text{ km s}^{-1}$ from Falco et al. (1999) and $2224 \pm 8 \text{ km s}^{-1}$ from Wegner et al. (2003) and the CO systemic velocity of $2225 \pm 15 \text{ km s}^{-1}$ (Young 2002). The CO and HI line widths also match well. The lower resolution map made from the combined AD and C array data gives the appearance of a smooth HI disk. The diameter of the HI emission is approximately $3.2'$. There

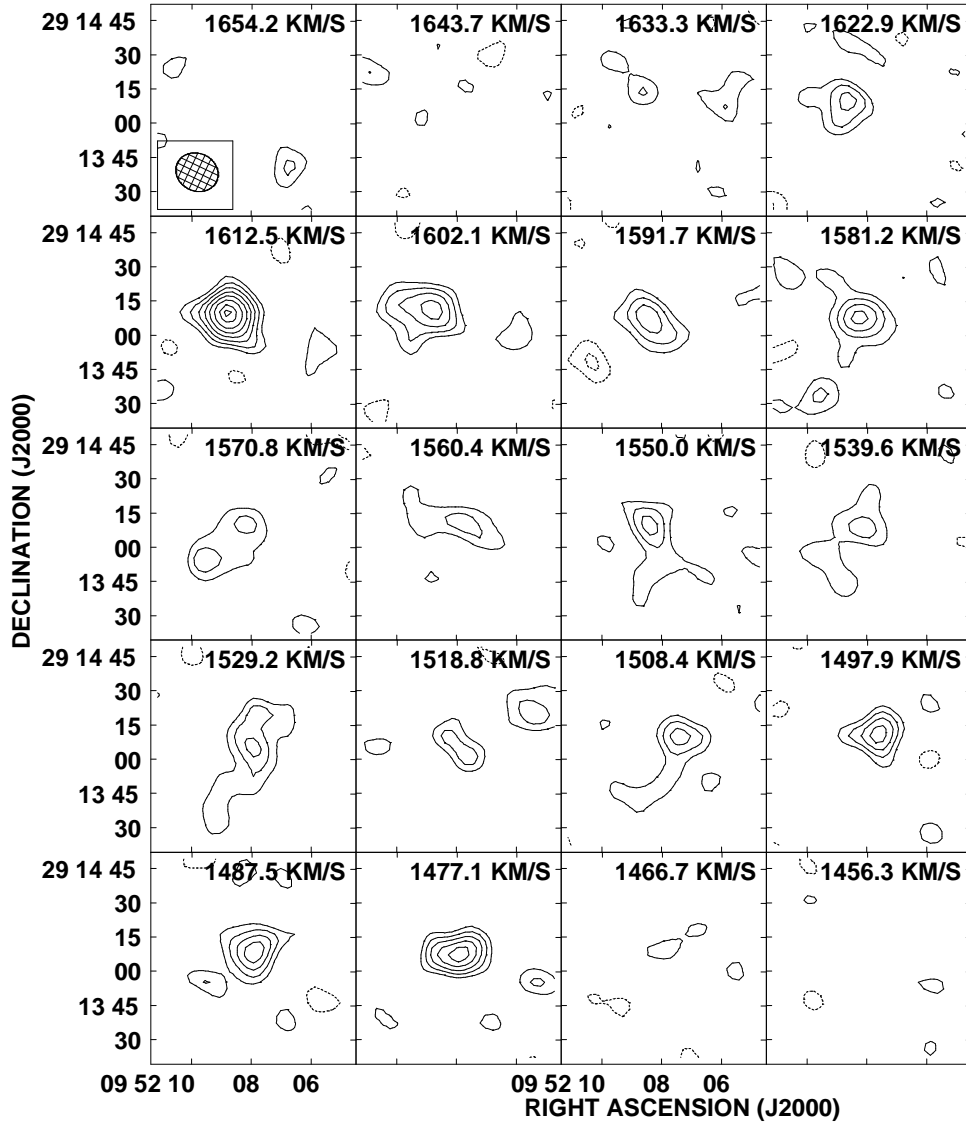


FIG. 13.— NGC 3032. Individual channel maps showing HI emission. Contour levels are $-3, -2, 2, 3, 4, 5, 6, 7, 8,$ and 8.5 times $0.6 \text{ mJy beam}^{-1} \sim 1\sigma$. The velocity of each channel (in km s^{-1}) is indicated at the top of each panel and the beam size in the first panel in the bottom left corner.

is a slight asymmetry in the HI distribution in that the spatial extent of the HI is larger on the eastern side of the galaxy (i.e. the contours of the integrated intensity are farther apart in the east). Like the CO emission, the HI in this galaxy is centrally peaked ($0.94 \text{ Jy beam}^{-1} \text{ km s}^{-1} = 9.1 \times 10^{20} \text{ cm}^{-2}$) and centered on the optical center of the galaxy. An inspection of the higher resolution C array data shows that the HI distribution is actually clumpy, with the overall appearance of a ring with a bright clump/disk of HI at its center. The HI ring begins at a radius of $\sim 45''$.

The HI detected sample galaxies fit well into the ATLAS^{3D} HI morphological classification scheme. The HI detected sample galaxies can be divided up into three categories: (D) Very extended regularly rotating HI disks (UGC 1503 and NGC 5666). (d) small regularly rotating HI disks that don't extend outside the optical body of the galaxy (NGC 2320, NGC 3032, and NGC 4150), and (u) unsettled HI morphologies (NGC 807 and NGC

3656). In the case of NGC 2320 we don't actually know the true extent of the HI emission, but we think it likely to be distributed like the CO, in a compact disk within the optical body of the galaxy. We prefer to classify NGC 807 as an intermediate between the D and u ATLAS^{3D} subclasses, because the kinematics of the HI are surprisingly regular despite obvious tidal features. We have no galaxies in our sample where the HI is found to be in small scattered external clouds. This could be due to the fact that the galaxies are biased toward the most CO rich objects.

None of the HI detected galaxies exhibit central HI holes. In all cases except for NGC 807 the HI and CO emission is centrally peaked. In the case of NGC 807 the HI and CO emission peaks are offset from the optical center but still coincide with each other. All of our sample HI detected galaxies have peak HI column densities at or above 10^{21} cm^{-2} except for NGC 4150 which peaks at $2.9 \times 10^{19} \text{ cm}^{-2}$. This is consistent with the peak HI

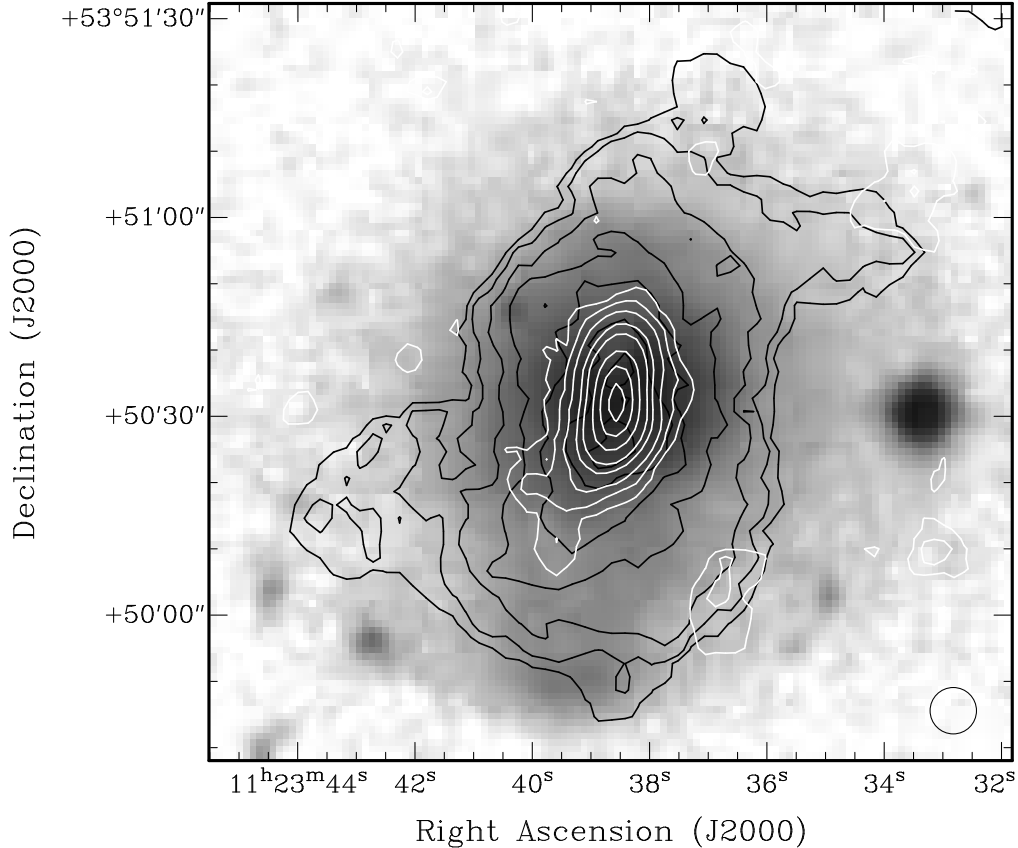


FIG. 14.— NGC 3656. HI and CO overlaid on an SDSS2 R band image. Solid black contours show the HI integrated intensity in units of 2%, 6%, 15%, 30%, 50%, 70%, and 90% of the peak ($0.32 \text{ Jy beam}^{-1} \text{ km s}^{-1} = 7.2 \times 10^{21} \text{ cm}^{-2}$). The HI map is constructed from B, C, and D array VLA data (Balcells et al. 2001). The circular ellipse shows the HI beam size. Solid white contours show the CO integrated intensity in units 2%, 5%, 10%, 20%, 30%, 50%, 70%, and 90% of the peak ($81.1 \text{ Jy beam}^{-1} \text{ km s}^{-1} = 4.7 \times 10^{22} \text{ cm}^{-2}$). The CO resolution is $7.8'' \times 6.2''$. The HI spectra and velocity field are published in Balcells et al. 2001.

column densities derived from the recent single dish surveys. Serra et al. (2012) note that the early-type galaxies in their sample with HI column densities of 10^{21} cm^{-2} all have the largest amounts of molecular gas, complex and prominent dust distributions, and strong evidence of star formation. The same is true for our HI detected sample galaxies except for NGC 2320 where there is no evidence of star formation (Young et al. 2007, Crocker et al. 2011). Serra et al. (2012) find that 50% of the very extended HI disks (class D) differ in orientation and kinematics from their stellar components, whereas the small HI disks (class d) are tightly coupled to their host galaxy. Our sample only exhibits the later trend. We see no misalignments between the HI major axis and the stellar isophotal major axis in any of our sample D galaxies. This could be an additional result of selection bias toward the CO richest objects or simply to the small sample size.

6. HI VERSUS CO KINEMATICS

Global kinematic position angles, inclinations, and systemic velocities are derived by fitting exponentially rising model rotation curves to the HI velocity fields depicted in the bottom right of Figures 7, 10, 12, 15, and 17 using the National Radio Astronomy Observatory’s AIPS task GAL. In the case of NGC 3656 we produced a HI velocity field by obtaining and re-reducing the VLA B and C array data using similar techniques as in Balcells et al.

(2001); the data are mapped with a Briggs robust parameter of 1.0 giving a beam size of $11.6'' \times 10.2''$ and an rms noise level $0.18 \text{ mJy beam}^{-1}$ in a 21 km s^{-1} channel. In the case of NGC 3032 the spatial resolution is sufficiently poor that the exponential fits are not robust. A solid body fit to their velocity fields proved more stable for NGC 3032. Estimates of the position angle of the kinematic major axis, inclination angle, and systemic velocities derived from these fits are consistent with values derived from the dust and CO maps of these five galaxies (Young et al. 2008; Young et al. 2009).

The GAL fits are weighted by the integrated intensity, so the fitted position angle is actually the kinematic axis at small radii. In order to get a good idea of how the position angle changes with radius, constant velocity rotation profiles were fitted to the velocity fields using concentric annuli. Annuli of $30''$ are used for NGC 807 and annuli $10''$ are used for the galaxies with smaller HI diameters. The constant velocity method also produces fitted position angles which agree with those derived from the CO to within a few degrees. The HI position angles of the major axis for all the galaxies discussed in this section are constant with increasing radii (within the margin of error), and never vary more than ~ 5 -10 degrees. There is a hint of a possible warp suggested by the slight presence of an integral sign shape in the zero velocity curve of the HI velocity field for NGC 3032 (Bottom left panel of Fig. 12). This integral sign feature may also be present in

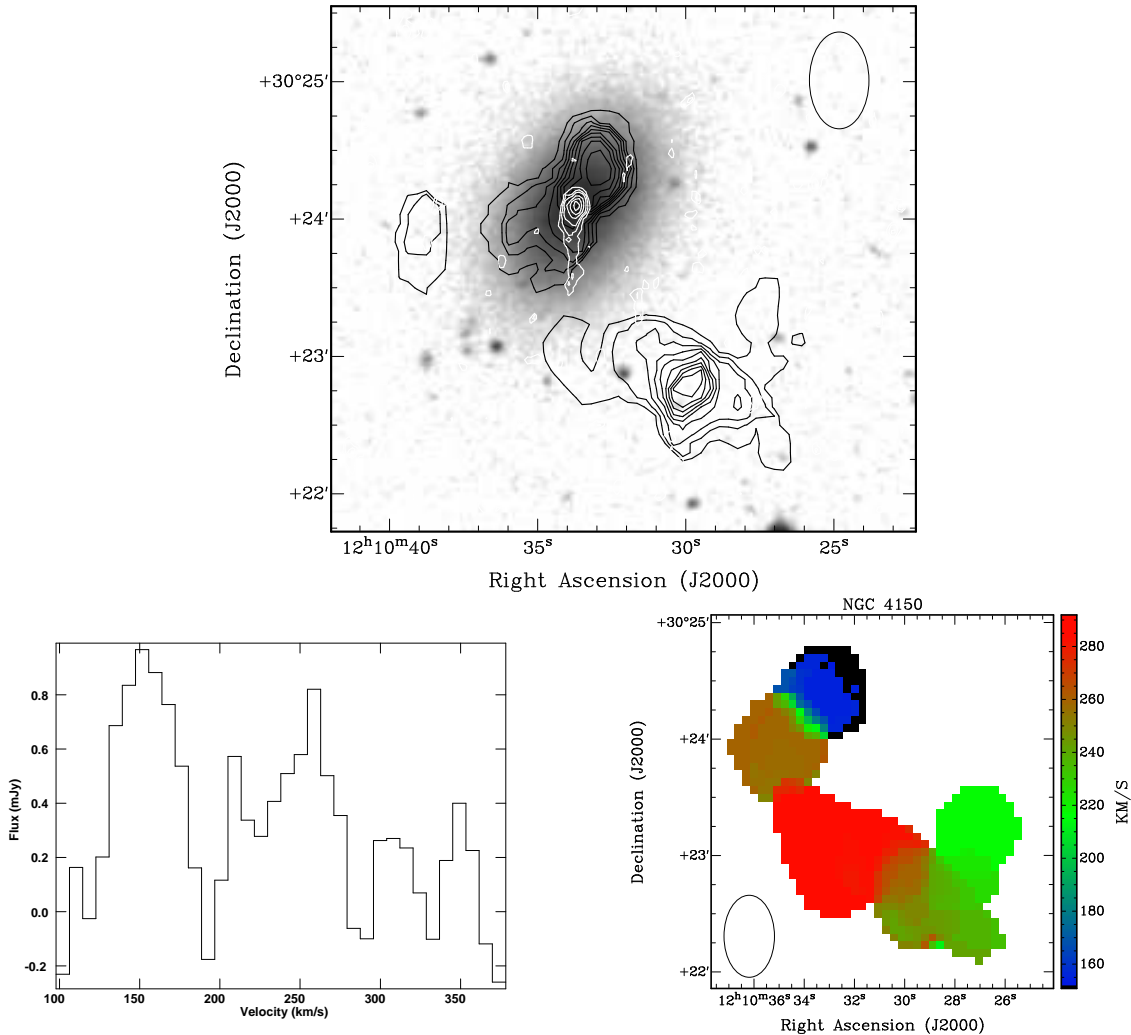


FIG. 15.— **Top:** NGC 4150. HI and CO. Solid white (positive) and yellow (negative) contours show the HI integrated intensity in units of 10%, 20%, 30%, 40%, 50%, 60%, 70%, 80%, and 90% of the peak ($28.9 \text{ mJy beam}^{-1} \text{ km s}^{-1} = 2.9 \times 10^{19} \text{ cm}^2$; Morganti et al. 2006). Solid white contours show the CO integrated intensity in units of 10%, 20%, 30%, 50%, 70%, and 90% of the peak ($17 \text{ Jy beam}^{-1} \text{ km s}^{-1} = 1.1 \times 10^{22} \text{ cm}^2$). The grey scale image is an SDSS2 R-band image. **Left bottom:** HI spectrum. Constructed in a similar manner to UGC 1503. This spectra was carefully made so as to no include any of the HI emission from the unknown HI source to the south east. **Right bottom:** Velocity Field. The HI intensity weighted mean velocity (moment 1) is shown in RGB color scale. Note that we include the velocity structure of both NGC 4150 and the unknown HI source to the south east. The black ellipse shows the HI beam size. The CO resolution is $8.5'' \times 5.1''$. The WSRT HI data are formally described in Morganti et al (2006) and Oosterloo et al (2010), but the spectrum and the kinematic figures have not been published so we show them here with the permission of the original authors.

TABLE 5
HI Kinematic Position Angles and Dynamical Masses

Galaxy	PA ($^{\circ}$)	i ($^{\circ}$)	$V \sin(i)$ (km s^{-1})	V (km s^{-1})	R_{HI} (kpc)	M_{dyn} $10^{10} M_{\odot}$	$\frac{M(HI)}{M_{dyn}}$	t_{orb} (10^8 yr)
U1503	-125	51(4)	144(5)	185(12)	16(1)	13	0.016	5.3
N807	146	65(6)	234(10)	258(17)	42(2)	65	0.016	10
N3032	90	44(2)	73(5)	105(8)	2.5(0.3)	0.78	0.010	1.8
N3656	191	74-90	213(11)	218(8)	8.0(0.2)	8.9	0.022	2.3
N5666	162	27(9)	105(11)	231(75)	14.5(0.9)	18	0.010	3.9

NOTE. — Position angles are derived using the AIPS task GAL.

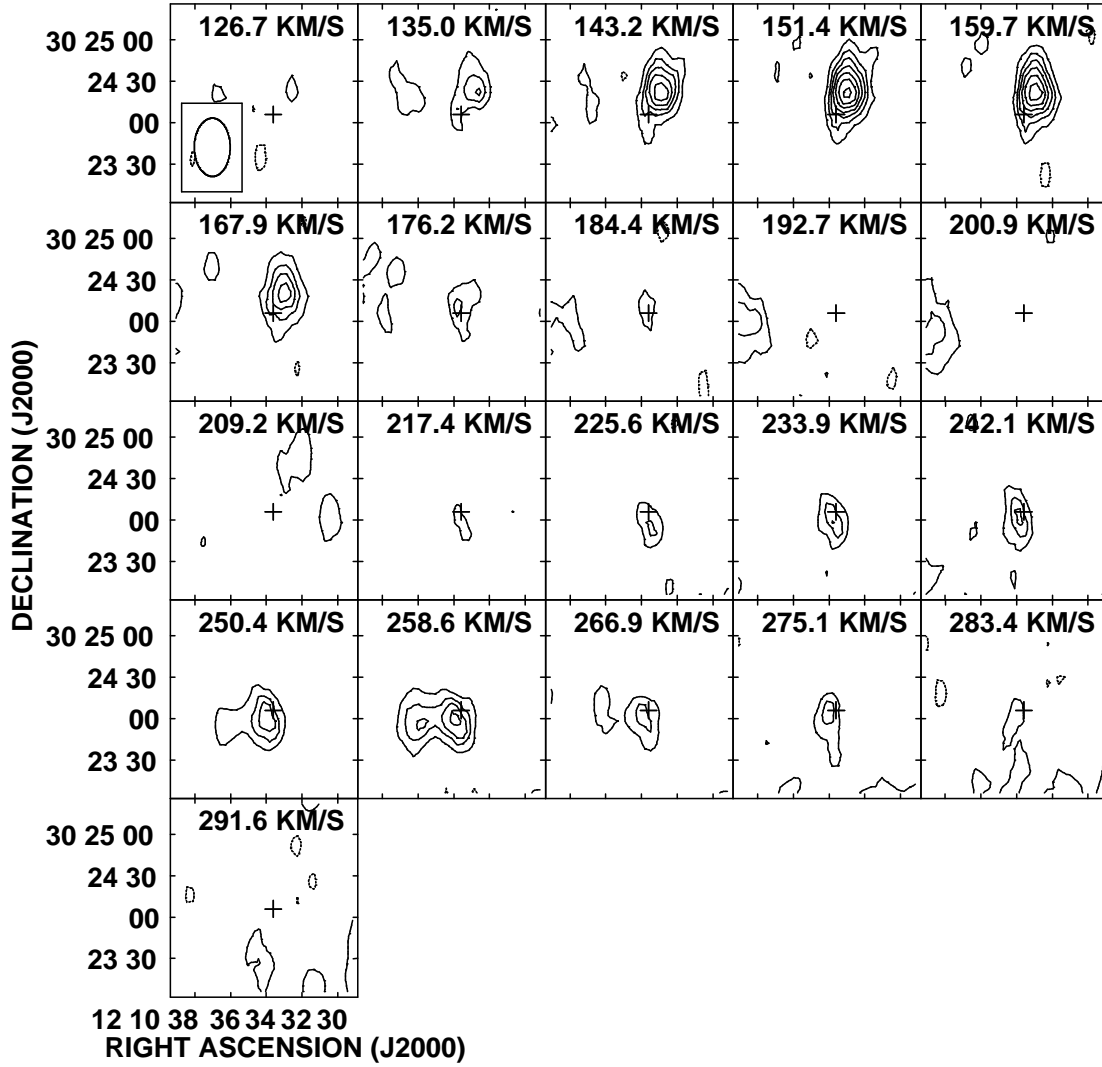


FIG. 16.— NGC 4150. Individual channel maps showing HI emission from the WSRT data (Morganti et al. 2006). Contour levels are $-4, -2.5, 2.5, 4, 5, 6, 7, 8, 9, 10$ and 11 times $0.11 \text{ mJy beam}^{-1} \sim 1\sigma$. The velocity of each channel (in km s^{-1}) is indicated at the top of each panel and the beam size in the first panel in the bottom left corner. We note here that the HI emission emission for NGC 4150 is made up of two components that are separated by $\sim 50 \text{ km s}^{-1}$ in velocity. The WSRT HI data are formally described in Morganti et al (2006) and Oosterloo et al (2010), but channel maps have not been published so we show them here with the permission of the original authors.

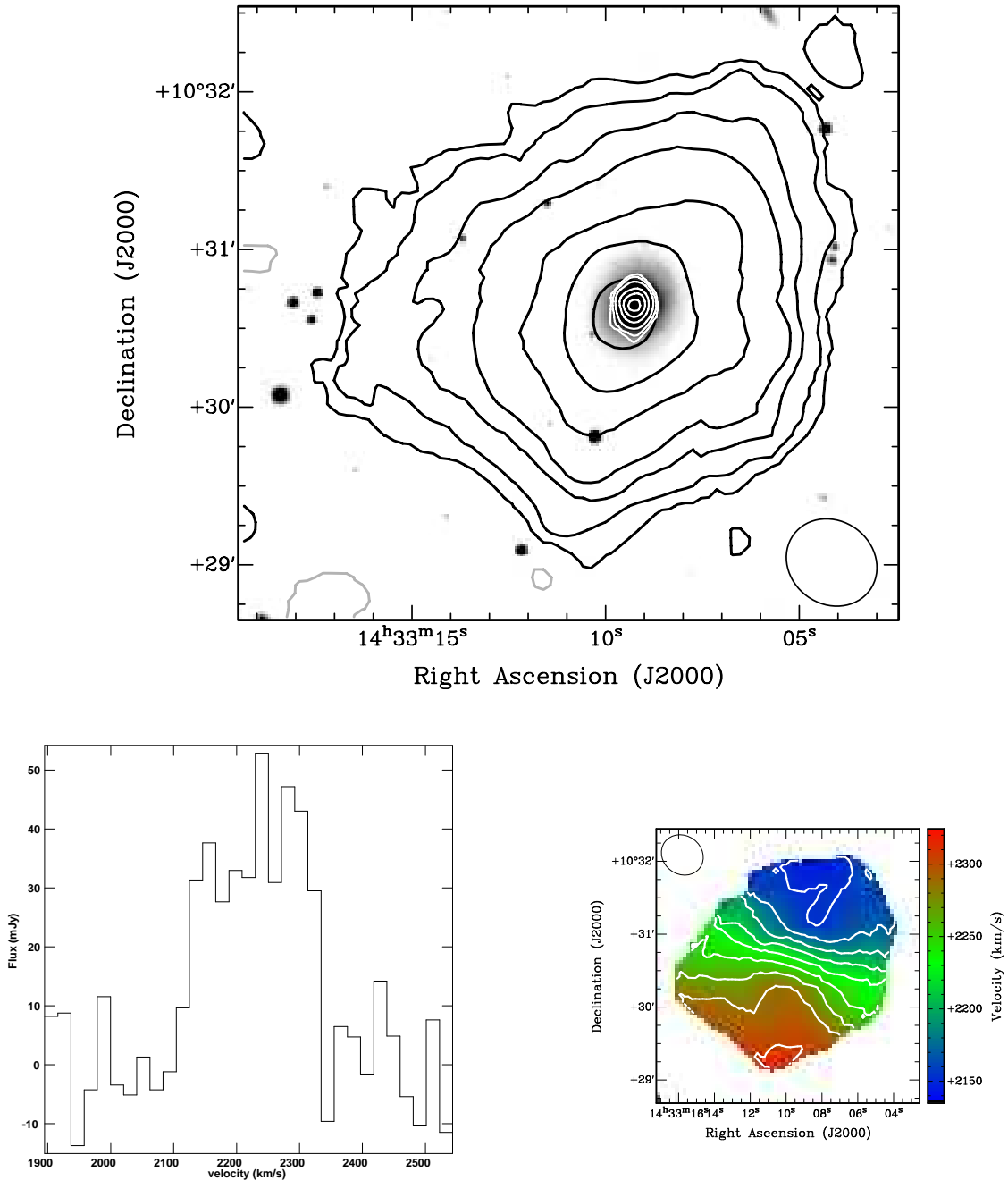


FIG. 17.— NGC 5666. **Top:** VLA C+D array HI overlaid with CO. Solid black (positive) and solid grey (negative) contours show the HI integrated intensity in units of -10% , -5% , 5% , 10% , 20% , 30% , 50% , 70% , and 90% of the peak ($0.94 \text{ Jy beam}^{-1} \text{ km s}^{-1} = 9.1 \times 10^{20} \text{ cm}^{-2}$). Solid white (positive) contours show the CO integrated intensity in units 15% , 20% , 30% , 50% , 70% , and 90% of the peak ($21.3 \text{ Jy beam}^{-1} \text{ km s}^{-1} = 7.5 \times 10^{21} \text{ cm}^{-2}$). The grey scale image is a WYIN 3.5 meter V band image. **Left bottom:** HI spectrum. Constructed in a similar manner to UGC 1503. **Right bottom:** Velocity Field. The HI intensity weighted mean velocity (moment 1) is shown in RGB color scale and in white contours from 2136 to 2324 in steps of 20 km s^{-1} . The black ellipse shows the HI beam size. The CO resolution is $8.3'' \times 6.1''$.

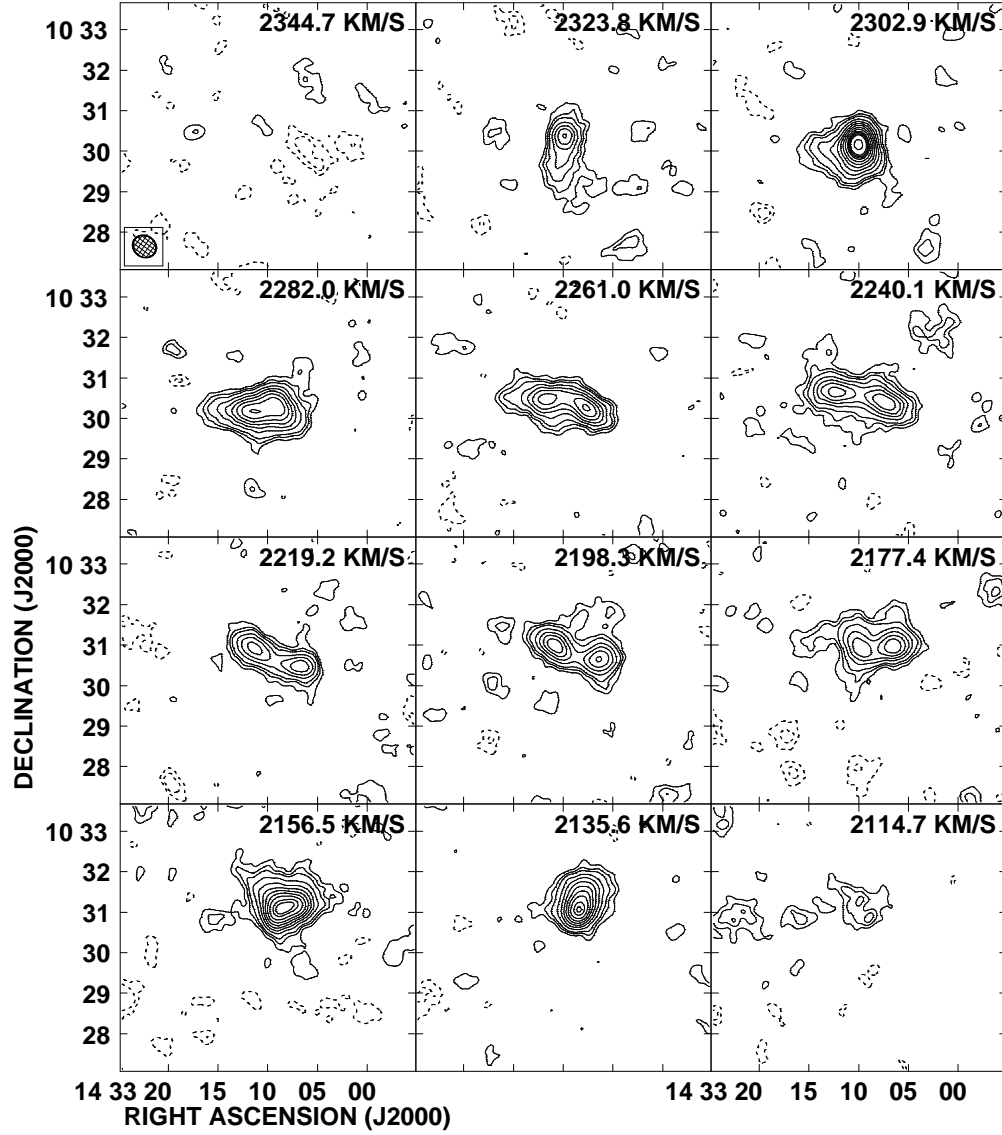


FIG. 18.— NGC 5666: Individual channel maps showing HI emission. Contour levels are $-3, -2, 2, 3, 4, 6, 8, 10, 12, 14, 16, 18, 19, 20, 21,$ and 24 times $0.5 \text{ mJy beam}^{-1} \sim 1\sigma$. The velocity of each channel (in km s^{-1}) is indicated at the top of each panel and the beam size in the first panel in the bottom left corner.

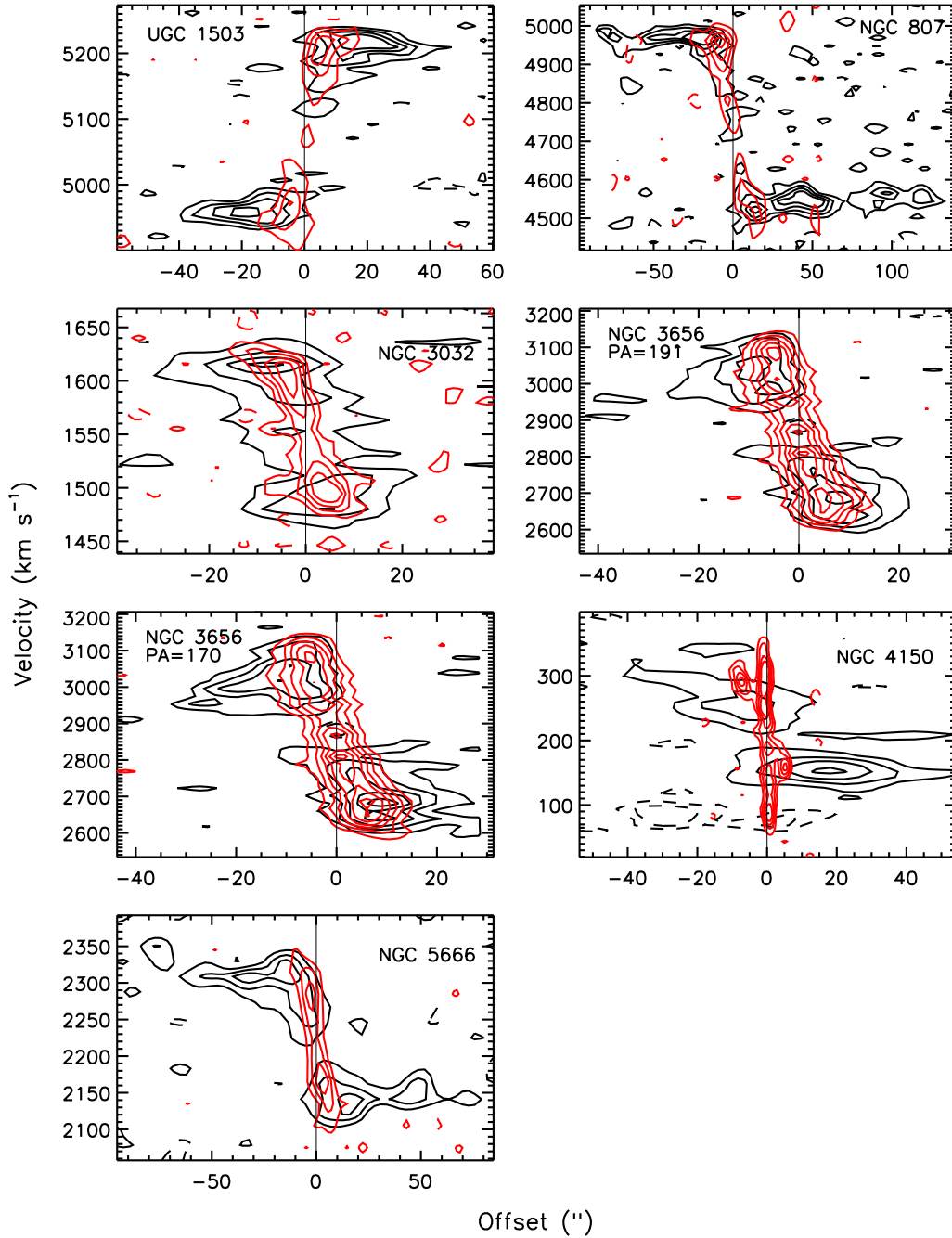


FIG. 19.— Position velocity curves. CO (red contours) and HI (black contours). The data cubes are sliced through the galaxy nucleus at the kinematic position angles derived from the GAL fits to the HI velocity maps (see Table 5 and section 6). The derived HI kinematic position angles are within a couple of degrees of the those derived from the CO data. The HI contour levels are all $(-2, 2, 4, 6, \dots)$ times the rms noise from Table 2. The CO contour levels are all $(-2, 2, 4, 6, \dots)$ times the rms noise in Tables 2, 3, and 3 of Young (2002), Young (2005), and Young et al. (2007), respectively. In the case of NGC 3656 the contours are multiplied by an additional factor of 1.3.

the CO velocity field of NGC 3032 (Young et al. 2008). However, the spacial and velocity resolution are poor for both HI and CO data sets.

In the case of NGC 4150 not only is the spacial resolution poor, but the distribution of the velocities is also highly non-uniform (see Figure 15c). The AIPS task GAL assumes a circularly rotating disk and so may not give correct results for the HI in NGC 4150. For this galaxy we employed the kinemetry techniques of Krajinovic et al. (2006) to measure the position angle as a function of radius. The measured position angles for NGC 4150 derived from this technique inside $12''$ are consistent with the stellar morphological and kinematic positions angles as well as the kinematic position angle derived from CO measurements.

Position-velocity plots for UGC 1503, NGC 807, NGC 3656, NGC 4150, and NGC 5666 are constructed using the kinematic centers and position angles derived from the model fits described above (see Figure 19). Both the HI (black contours) and CO (red contours) data cubes are sliced through the galaxy nucleus at the kinematic position angle listed in Table 5. The position-velocity diagrams for UGC 1503, NGC 807, and NGC 3032 show steeply rising, approximately solid body rotation regions in their centers followed by a flattening at the edges of the HI distribution. In the case of NGC 5666 the position-velocity plot represents the superposition of two separate components, an inner HI disk (radius of $<25''$) and an outer HI ring (radius of $>25''$). The HI in the inner ring does not appear to extend past the region of solid body rotation while the material in the outer ring has only a flat constant velocity component. It is interesting to note that the material in the ring appears to be rotating 20 km s^{-1} or 15% slower than the material at the edge of the inner HI disk. The appearance of slower rotation of the ring could be due to a central mass concentration as is observed for the Milky Way or perhaps to a change in the orientation of the velocity field. However, the GAL constant velocity fits for NGC 5666 show that the position angle in the vicinity of the ring does not change more than a few degrees from that of the disk component. Thus, it is not clear whether these two components are kinematically distinct.

In the case of NGC 3656 we use two position angles to construct the position-velocity plots in Figure 19. The angle of 191 degrees is derived from the CO map, weighted towards the inner part of the CO, and there is some evidence of a warp as the outer regions tend towards position angles less than 180 degrees. Balcells et al. (2001) use 170 degrees and that position angle also cuts through a prominent HI shell in the southern part of the galaxy. The resulting position-velocity overlays produce obvious signatures of non-circular gas motions in the outer portions of the HI disk. As in the other cases the CO does not appear to extend past the solid body portion of the rotation curve and appears to be for the most part kinematically settled. The HI also appears to be kinematically settled within the CO radius.

The position-velocity overlays show that the kinematics of the CO and the HI match for UGC 1503, NGC 807, NGC 3032, NGC 3656, and NGC 5666 which strongly suggests a common origin for the two gas phases in these five galaxies. The position-velocity plot of NGC 4150 shows that the HI and CO share the same sense of ro-

tation, but have very different line widths. This is likely due to the fact that much of the HI in this galaxy is currently unsettled due to a recent interaction (section 5). We do not have an HI velocity map for NGC 2320, however its gas morphology as discussed in section 5 also implies a common origin between both gas phases.

The dynamical mass interior to the HI disk's outer edge can be calculated using the observed gas velocities:

$$M_{dyn} = (2.33 \times 10^5 M_{\odot}) V^2 R \quad (1)$$

where R is the radius of the outer edge in kpc and V is the observed velocity in km s^{-1} , corrected for inclination. This is assuming that the gas disks are intrinsically circular, and that the gas itself moves along circular orbits. The implied dynamical masses (Table 5) range from a few $\times 10^9 M_{\odot}$ to a few $\times 10^{11} M_{\odot}$ interior to the edge of the HI disk, and the observed masses of atomic gas are a few percent of these dynamical masses. Table 5 also gives the orbital time for gas at the edges of the HI disks.

7. DISCUSSION

7.1. The Effect of Environment on the HI content

As in other recent HI early-type surveys we find that the most HI-deficient galaxies either reside in cluster/group environments, show indications of recent interactions or both. The most HI rich galaxies reside in the field, but several of these galaxies also show indications of recent interactions.

The deficiency of atomic gas in clusters galaxies is thought to be due to mechanisms such as (1) tidal interactions, (2) ram pressure (Gunn & Gott 1972), (3) turbulent/viscous stripping (Nulsen 1982), and (4) fast evaporation of the atomic gas due to the presence of a hot intracluster medium (Grossi et al. 2009). Grossi et al. (2009) suggest that these mechanisms would also aid in limiting the number of HI rich dwarfs in clusters, thus limiting the available reservoirs of gas from which other larger galaxies can feed. In the three HI-undetected lenticulars (NGC 4459, NGC 4476, NGC 4526) there is no indication in the CO or optical data of a recent tidal interaction (Young 2002, Young et al. 2008). Therefore, we conclude that the HI in these galaxies has most likely been removed by one or a combination of the last three mechanisms mentioned above. Additionally, current photodissociation models imply that a sudden increase in pressure will increase the gas surface density such that large portions of a galaxy could spontaneously become molecular without converting the diffuse gas to self-gravitating clouds (e.g. Elmegreen 1993). This is perhaps a plausible explanation for why no HI is detected over the entirety of the CO disks of these three galaxies. We will explore this possibility in more depth in paper II (Lucero & Young in prep).

NGC 4150 is detected in HI despite being a Coma group member. The presence of HI in this galaxy can be explained by the fact that it resides near the edge of the cluster where the ICM densities are probably lower (i.e. ram pressure and evaporation are much less effective), and the population of HI-rich dwarfs is probably higher. Indeed it appears likely that NGC 4150 is accreting gas from a nearby low surface brightness dwarf galaxy. The HI surface densities of both NGC 4150 and the unknown HI source peak at $\sim 0.2 M_{\odot} \text{ pc}^{-2}$ (corrected for helium and

inclination) which is more than 25 times smaller than the lowest peak surface density of the HI detected field galaxies. This implies that the stripping/evaporation mechanisms are either still affecting the gas content at a reduced efficiency or only existed for a shorter period of time compared to those cases where the HI has been completely stripped.

Many of the same mechanisms discussed above could also be at work in group environments, and could also explain the HI deficiency in NGC 83 and NGC 2320. Both galaxies are located relatively nearby to strong sources of X-ray emission. NGC 83 is a member of the NGC 83 Group. This group is very near (in velocity and spatially) to the galaxy cluster PCC S49-147. A GIS X-ray mosaic image shows that the NGC 83 group could be embedded in the diffuse X-ray intracluster medium associated with PCC S49-147 (Nakazawa et al. 2007a). NGC 2320 is about 2° or 2.9 Mpc in projection from NGC 2329 which lies at the center of the Abell 569 cluster. The Abell 569 cluster was recently observed with the Einstein satellite (Burns et al. 1994). The X-ray emission in this cluster is relatively compact, is quite bright, and is centered on NGC 2329.

NGC 83 and NGC 2320 are the most luminous galaxies in the present sample. Grossi et al. (2009) suggest that the presence of a hot X-ray ISM in luminous early-type galaxies may prevent an atomic phase from forming altogether or cause the HI (whether it originates from mass loss or accretion) to evaporate. Unfortunately, neither NGC 2320 and NGC 83 have been searched deeply for hot gas, and no evidence of a hot ISM has been reported for either galaxy in the literature outside of what has been discussed above. The blue luminosities of NGC 83 and NGC 2320 are well in the range in which O’sullivan et al. (2001) find copious amounts of hot gas. The lower luminosity sample galaxies live in the lower range where the X-ray luminosity is dominated by emission from X-ray binary systems rather than hot gas (see Figure 9 of O’sullivan et al. 2001).

Interestingly, the CO properties of the HI-deficient galaxies do not differ that much from their field counterparts. The only difference worth mentioning is that the cluster/group galaxies have larger peak H_2 surface densities than both the group and field galaxies. One might expect the density of the molecular gas in the center of cluster/group galaxies to be increased due to ICM/ram pressures (Nakanishi et al. 2006). We will explore the effects of external pressures on the gas surface density in depth in paper II (Lucero & Young in prep). Of course the larger peak H_2 surface densities could be a resolution effect as all of the cluster galaxies are 2 to 5 times nearer than the other galaxies in the sample.

7.2. *The Origin of the Cold Gas in Early-Type Galaxies*

We find an overwhelming amount of evidence that suggests that both the neutral hydrogen and molecular gas in our early-type galaxy sample share a common origin be it external or internal. The kinematics of the HI and CO gas phases in the sample galaxies are remarkably similar. The HI and CO line widths, intensity peaks, and kinematic position angles match in all cases. We find that if the HI is in a relaxed disk, so is its CO. Alternatively, if the HI appears disturbed, so does its CO. Thus, our results are consistent with the ATLAS^{3D} volume limited

survey which also find that the two gas phases always exhibit the same kinematics. Other early-type galaxies with differing CO and HI linewidths (e.g. Welch & Sage 2003; Sage & Welch 2006; Sage et al. 2007; Welch et al. 2010) are probably cases in which the HI is either still falling in or being affected by tidal or ram pressure stripping. The existing interferometric data shows that the HI is often extended over tens of kiloparsecs while the CO is confined to the inner 1-4 kpc. The kinematics of the HI and CO always match where the two phases overlap. Outside the CO radius the HI often exhibits a range of other morphologies and kinematics.

As in the previous HI surveys, the total gas content ($HI+H_2$), HI content, and H_2 content only weakly correlate with galaxy luminosity. This is an indication that the cold gas may have an external origin. Indeed, a large number (45%) of the sample galaxies show evidence that their cold gas has been obtained or is currently being accreted from outside sources. These include NGC 2320, NGC 3032, NGC 3656, NGC 4150, and NGC 4476. The most obvious cases are NGC 3032 and NGC 4476. The cold gas systems (HI and CO) in these two galaxies are counter-rotating with the bulk of the stars, and therefore an internal origin can be ruled out (Young et al. 2008; Crocker et al. 2010). Additionally, small extensions of HI and CO in NGC 3032 and NGC 4150 oriented in roughly the same direction imply that this gas is actively falling onto these galaxies. NGC 2320 contains an absorbing HI complex and an extension of CO emission which have similar velocities redshifted with respect to the systemic velocity indicating gas is actively falling in toward the galaxy. The radio continuum emission in NGC 2320 is thought to be powered by an AGN. Perhaps the cold gas in NGC 2320 is helping to fuel the central AGN activity (Young 2005). Tidal features (optical and HI) and the non-circular motions implied by the velocity structure of the HI in NGC 3656 also suggest that the cold gas in this galaxy has been acquired during a recent interaction (Bacells et al. 2001).

The origin of the cold gas in NGC 83, UGC 1503, NGC 807, NGC 4459, NGC 4526, and NGC 5666 is less clear. The kinematics of the HI and or CO disks in the field early-types UGC 1503 and NGC 5666 suggest that the gas/dust disks in these systems are well settled into dynamic equilibrium. The orbital timescales at the edge of the HI disks in UGC 1503 and NGC 5666 are 0.5 Gyr and 0.4 Gyr respectively. If the cold gas in these two galaxies was acquired from an external source it must have occurred several orbital timescales ago. There is no overwhelming evidence for an outside origin of the molecular gas for the cluster/group galaxies NGC 83, NGC 4459, and NGC 4526 except perhaps slight asymmetries in the CO distributions of NGC 4459 and NGC 4526 (Young et al. 2008). The generally symmetric appearance of the optical images of these three galaxies also suggests that it has been well over a Gyr since any mergers, if any, have occurred. One then might conclude that their cold gas originated solely from mass loss. However, Davis et al. (2010) suggest that the tell tale signatures of an external origin for the cold gas may get erased by environmental processes such as ram pressure or by galaxy wide processes in the most massive objects such as NGC 83. If true, prograde gas cannot completely rule out an external origin of the cold gas in these particular galaxies.

The HI in NGC 807 appears to be in a relaxed disk out to a radius of $\sim 1.4'$, and then outside this radius the HI appears to be tidally disrupted. A deep optical image taken by the WYIN telescope also shows the presence of faint stellar tidal arms oriented in a similar manner to that of the HI tidal features (bottom panel of Fig 9). The kinematics of the HI and CO in NGC 807 are surprisingly regular. The uniformity of the kinematics probably mean that the cold gas was already distributed in a relaxed regular rotating structure like those observed in NGC 5666 and UGC 1503 before the interaction occurred. This of course does not rule out the possibility that the cold gas in NGC 807 was acquired a few orbital timescales before the most recent interaction. A better way to distinguish between external and internal gas origins would be to look for significant differences in angular momentum between the cold gas and the stars. Unfortunately, we lack the necessary stellar kinematic information to carry out this type of analysis for these particular galaxies.

8. CONCLUSIONS

In this paper we present an analysis of new VLA and archive HI observations of 11 CO rich early-type galaxies as well as a preliminary comparison between the HI and CO morphologies and kinematics. The new HI observations have 2 to 16 times better resolution than that of the recent volume limited HI surveys of early-type galaxies. In summary:

Six of the eleven sample galaxies (UGC 1503, NGC 807, NGC 2320, NGC 3032, NGC 3656 and NGC 4150) are detected in HI; the other five are not, even though they have strong CO detections. The HI detected galaxies have a wide range of HI masses (1.4×10^6 to $1.1 \times 10^{10} M_{\odot}$). There does not appear to be any correlation between the HI mass or morphology (E versus S0).

HI absorption is detected for NGC 2320. The peak of this absorption is red shifted with respect to the optical systemic velocity by 60 km s^{-1} and may be associated with a small extension of CO emission which is at a similar offset velocity as the HI. We suggest that the absorbing HI and the CO extension are probably part of the same gas structure which is actively falling toward the center of the galaxy.

The HI in UGC 1503, NGC 3032, NGC 4150, and NGC 5666 is distributed in disk-like structures in regular rotation with diameters of a few to 16 kpc. The HI emission for these galaxies peaks at the disk center ($5 - 9 \times 10^{20} \text{ cm}^{-2}$). There are no kpc sized HI holes like those observed in early-type spiral galaxies. NGC 807 and NGC 3656 have a significant amount of HI located in tidal arms far from the main disk. The cold gas kinematics of NGC 807 are surprisingly regular despite the fact that the gas has recently been disturbed.

The relatively high resolution of the HI maps presented in this work enable more detailed comparisons of CO and HI kinematics than have previously been possible for early-type galaxies. In the regions where both phases are detected, they show identical kinematics within our measurement errors. In the three cases where HI traces a clear turnover in the circular rotation speed, the molecular disks extend out to the turnover (so they would be

useful in a Tully-Fisher analysis) but not far beyond that point (so the molecular gas is strongly concentrated in the solid-body part of the rotation curve).

A little over half of the early-type sample galaxies show evidence that their cold gas has been obtained or is currently being accreted from outside sources. We find no evidence in the present early-type galaxy sample to support the suggestion that the HI and CO have different origins. There is also no indication that the origin of the cold gas is dependent on galaxy morphology (E versus S0), stellar luminosity or environment.

As in the recent volume limited surveys of early-type galaxies, there is a clear correlation with environment and HI. All of the HI non-detected galaxies reside in group or cluster environments. The galaxy with the smallest detected HI mass (NGC 4150) resides at the edge of the Virgo Cluster where ICM densities are expected to be low.

Overall, the results of these observations are consistent with the recent HI surveys which also find a mix of HI morphologies and masses, low HI peak surface densities, and a paucity of HI in early-type galaxies which reside in high density environments.

The fact that all of the isolated field galaxies are detected in HI is consistent with the assumption that once an early-type has obtained some cold gas, it is much easier to hold on to it in low density environments. The very regular kinematics and highly extended HI disks in UGC 1503 and NGC 5666 imply that their gas systems are relatively old, at least a few orbital time scales (on the order of a few Gyrs). NGC 807, NGC 3032, and NGC 3656 show indications that their cold gas has recently been acquired or disturbed. This is good evidence to support the proposition that there is still a significant amount of cold gas in field environments on which early-type galaxies can feed.

The conclusions presented in this work are based on a relatively small sample of galaxies biased toward early-type galaxies known to contain substantial amounts of molecular gas. Clearly, we must extend our analysis to a much larger and more homogenous sample of early-type galaxies.

We thank the reviewer for his/her thorough review and highly appreciate the comments and suggestions, which significantly contributed to improving the quality of the publication. We are grateful to Jacqueline van Gorkom for providing the HI map and of NGC 3656 as well as Raffaella Morganti and Tom Oosterloo for providing the WSRT HI map and image cube for NGC 4150. This work is based on observations collected with the Very Large Array operated by the National Radio Astronomy Observatory. The National Radio Astronomy Observatory is a facility of the National Science Foundation operated under cooperative agreement by Associated Universities, Inc. This research has also made use of the NASA/IPAC Extragalactic database (NED) which is operated by the Jet Propulsion Laboratory, California Institute of Technology, under contract with the National Aeronautics and Space Administration. This work is partially supported by NSF grants AST-0507432 and AST-1109803. *Facilities:* VLA.

TABLE 6
HI properties of Galaxies in the Field of NGC 2320 and NGC 3032

Galaxy	morph	RA (J2000)	DEC (J2000)	V_{helio} (km s^{-1})	D (Mpc)	$S_{\nu, HI}$ (Jy km s^{-1})	M(HI) ($\times 10^8 M_{\odot}$)
NGC 2321	SBa	07h05m59.0s	50d45m22s	6318(13)	87	2.3(0.2)	41
KUG 0950+295	Irr	09h52m57.3s	29d18m38s	1628(42)	22	0.94(0.10)	1.1
DS96 0949+2935 ^a	dwarf	09h52m43.8s	29d20m53s	1456(16)	20	1.2(0.1)	1.1
Unknown ^b	?	09h52m52.2s	29d21m08s	1602(10)	22	0.2(0.02)	0.23

NOTE. — Morphological types, positions and systemic velocities are taken from NED if available. The distance is calculated from the systemic velocity and $H_0 = 73 \text{ km s}^{-1} \text{ Mpc}^{-1}$.

No correction is made for the presence of helium or inclination effects in the HI masses.

^a Systemic velocity measured from the HI line observations with the Arecibo 300 meter telescope (Duprie & Schneider 1996)

^b Position and systemic velocity measured from the HI line from the VLA C array observations presented in this paper.

APPENDIX

HI DETECTION OF SOURCES IN THE VICINITY OF NGC 2320 AND NGC 3032

In this section we report new VLA observations of several HI sources detected in the fields of NGC 2320 and NGC 3032. HI images, spectra, velocity fields, and individual channel maps can be found in Figures 20-26. The properties of the HI detections for these sources can be found in Table 6. A description of the data reduction can be found in section 3. All of these field sources are outside the field of view the BIMA CO observations of Young (2002, 2005) and Young et al. (2008).

NGC 2321

NGC 2321 is classified as a barred spiral galaxy in the RC3 catalogue. NGC 2321 is also a likely member of the Abell 596 cluster as its systemic velocity (6318 km s^{-1}) is well within the velocity dispersion of that cluster ($\sim 300 \text{ km s}^{-1}$). NGC 2321 is about $10'$ from NGC 2320 and about $8'$ from the cluster center in projection.

Figures 20 and 21 show the integrated intensity, the HI spectrum, velocity map, and the individual channel maps. The total HI flux is $2.6 \pm 0.3 \text{ Jy km s}^{-1}$ which translates to an HI mass of $4.1 \times 10^9 M_{\odot}$. The HI emission is detected over $301 \pm 11 \text{ km s}^{-1}$ centered on a systemic velocity of $6316 \pm 11 \text{ km s}^{-1}$ which gives a circular velocity of $V_{circ} \sin i = 151 \text{ km s}^{-1}$. This flux is consistent with single dish HI observations made with the meridian transit Nancay radiotelescope (Theureau et al. 1998) which quote an HI flux of $2.3 \pm 1.0 \text{ Jy km s}^{-1}$.

The channels maps show the characteristic butterfly pattern, and so the HI is probably distributed in a disk in semi-regular rotation. The HI is not centrally peaked, but peaks inside the disk. In the northeastern part of the disk there is a marginally resolved region of what appears to be HI in absorption (peak $-68 \text{ Jy beam}^{-1} \text{ km s}^{-1}$ at RA 7h 05m 56.357s Dec 50d 45m 35.30s). However, there is no evidence of any continuum source at the position of the absorption. There is a 2.9 mJy source listed in the NVSS about $1.4'$ to the northeast (Condon et al. 1998) which is clearly visible in a radio continuum maps made from the new VLA data, but can't be associated with the absorption. An inspection of the channel maps shows that there is significant negative emission in only two channels, and these channels are quite far apart in velocity space. We conclude that the negative emission is a 5 sigma artifact due to problems with imaging a source that is located significantly far from the pointing center and continuum subtraction (similar to those of NGC 4459, see section 2.3). We attempted to use various other continuum subtraction techniques, but are unable to produce a data cube without the artifact. It is surprising that all of the flux is recovered, despite the artifact.

KUG 0950+295 and DS96 0949+2935

We detect three distinct sources of HI emission about $12'$ to the Northeast of NGC 3032 in projection. These include:

KUG 0950+295- Classified as an irregular galaxy in the RC3 catalogue, it is located $13'$ to the northeast of NGC 3032 in projection. The total HI flux is $0.94 \pm 0.10 \text{ Jy km s}^{-1}$, and it is detected over $100 \pm 11 \text{ km s}^{-1}$ centered on a systemic velocity of $1650 \pm 11 \text{ km s}^{-1}$ which gives a circular velocity of $V_{circ} \sin i = 50 \text{ km s}^{-1}$. This flux is consistent with single dish HI observations made with the 100-m radio telescope at Effelsberg which quote an HI flux of 1.2 Jy km s^{-1} detected over 90 km s^{-1} centered on a systemic velocity of $1638 \pm 8 \text{ km s}^{-1}$ (Huchtmeier et al. 2000). We derive a distance of 22 Mpc using the systemic velocity derived from the 100-m observations and $H_0 = 73 \text{ km s}^{-1} \text{ Mpc}^{-1}$. Using this distance and our flux we calculate an HI mass of $1.1 \times 10^8 M_{\odot}$. The HI in this galaxy is centrally peaked. As in NGC 3032 the HI distribution is only a few beams across and so is not well resolved. An inspection of the HI velocity field shows that the emission exhibits solid body rotation with only a slight suggestion of becoming flat near the outer parts of the HI distribution.

DS96 0949+2935- The HI emission associated with DS96 0949+2935 has a double horned HI profile indicative of a rotating disk galaxy, but only a few faint features are visible in the POSS2 images which make a clear classification difficult (Duprie & Schneider 1996). The HI distribution is fairly well resolved and the velocity field clearly turns over at the edge of the disk suggesting the HI is in a rotating disk. The total HI flux of DS96 0949+2935 is $1.2 \pm 0.1 \text{ Jy km s}^{-1}$, and is detected over $100 \pm 11 \text{ km s}^{-1}$ centered on a systemic velocity of $1450 \pm 11 \text{ km s}^{-1}$ which gives a circular

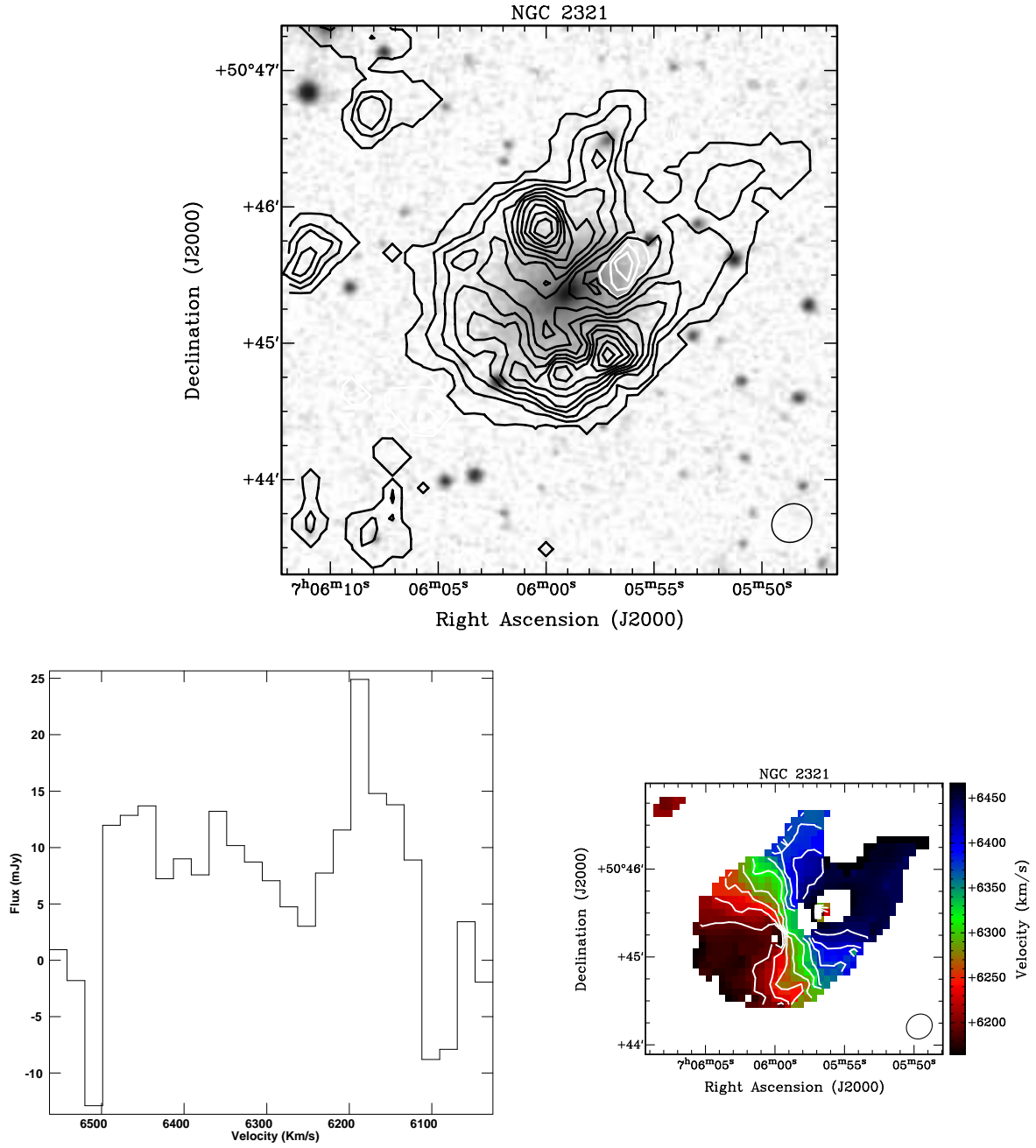


FIG. 20.— **Top:** Solid black (positive) and solid white (negative) contours show the HI integrated intensity in units of -20% , -10% , -1% , 1% , 10% , 20% , 30% , 40% , 50% , 60% , 70% , 80% and 90% of the peak ($0.94 \text{ Jy beam}^{-1} \text{ km s}^{-1} = 9.1 \times 10^{20} \text{ cm}^{-2}$). The grey scale image is an SDSS2 red band image. **Left bottom:** HI spectrum. Constructed in a similar manner to UGC 1503. **Right bottom:** Velocity Field. The HI intensity weighted mean velocity (moment 1) is shown in RGB color scale and in white contours from 6150 to 6450 km s^{-1} in steps of 21 km s^{-1} . The black ellipse shows the beam size.

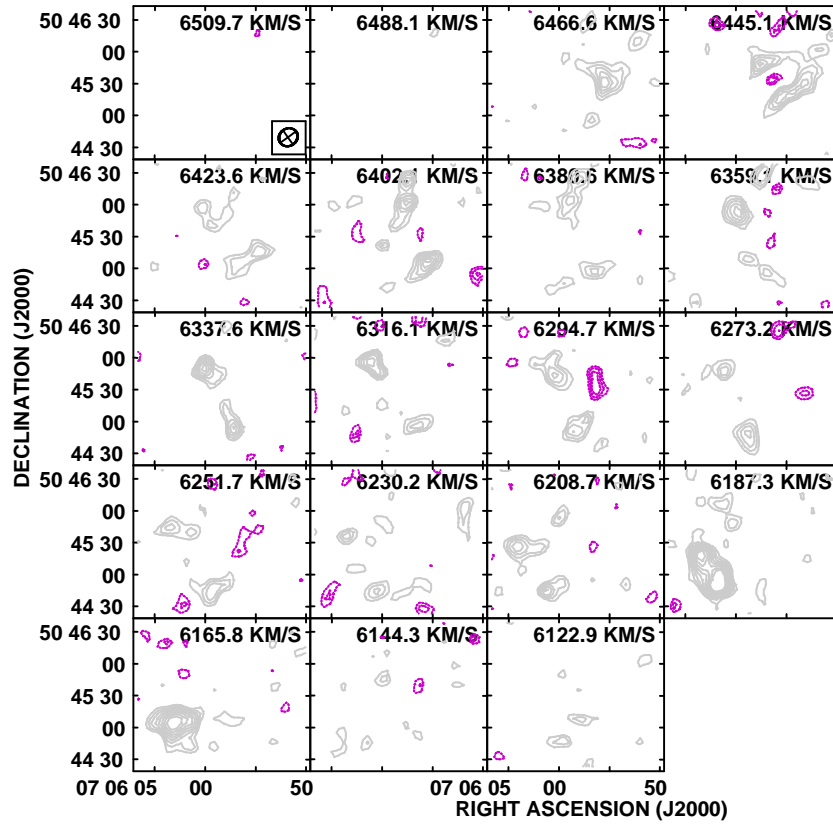


FIG. 21.— NGC 2321: Individual channel maps showing HI emission. Contour levels are -5, -4, -3, 3, 4, 5, 6, 7, 8, 9, and 10 times $0.3 \text{ mJy beam}^{-1} \sim 1\sigma$. Negative contours are purple. The velocity of each channel (in km s^{-1}) is indicated at the top of each panel and the beam size in the first panel in the bottom left corner.

velocity of $V_{\text{circ}} \sin i = 50 \text{ km s}^{-1}$. This is consistent with a Arecibo 300 meter telescope flux of 1.3 Jy km s^{-1} detected over 106 km s^{-1} centered on a systemic velocity of 1456 km s^{-1} (Duprie & Schneider 1996).

Unknown source- A faint source of HI emission located $\sim 1'$ away from DS96 0949+295 in projection at RA 09h 52m 41.78s and Dec 29d 21m 44.75s. This faint source is probably associated with a low surface brightness dwarf galaxy that appears as a faint smudge in the POSS2 image. The HI flux of the fainter source has a flux of $0.2 \pm 0.02 \text{ Jy km s}^{-1}$, and is detected over $33 \pm 11 \text{ km s}^{-1}$ centered on a systemic velocity of 1602 km s^{-1} . The systemic velocity of this faint object puts it 2 Mpc behind DS96 0949+2935. There is no clear indication from the VLA data or in the optical images that might suggest that this unidentified source is interacting with DS96 0949+2935. There are no other HI detections of this faint source mentioned in the literature.

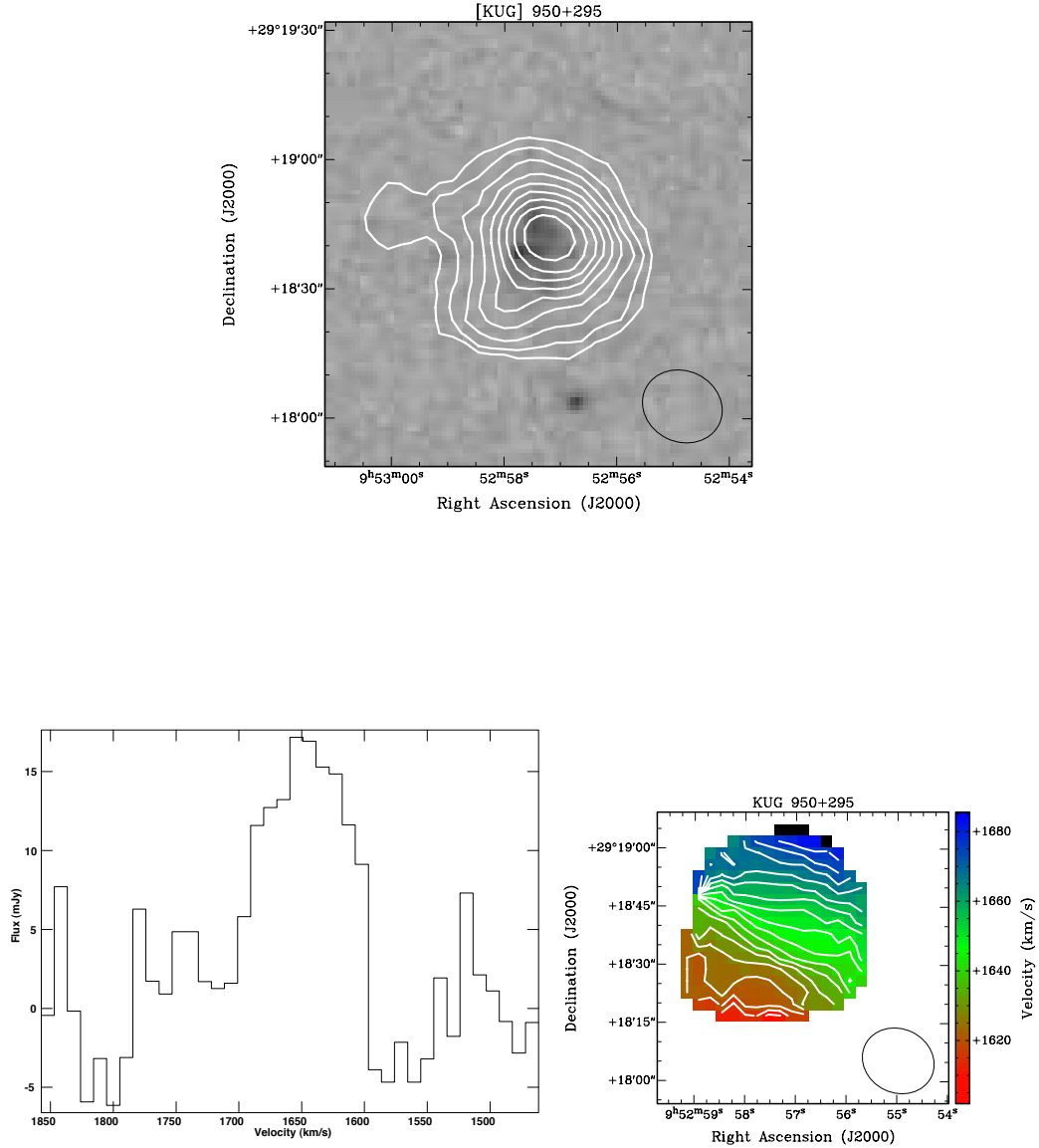


FIG. 22.— **Top:** Solid black (positive) and solid grey (negative) contours show the HI integrated intensity in units of -20% , -10% , -1% , 1% , 10% , 20% , 30% , 40% , 50% , 60% , 70% , 80% and 90% of the peak ($0.33 \text{ Jy beam}^{-1} \text{ km s}^{-1} = 1.1 \times 10^{21} \text{ cm}^{-2}$). The grey scale image is an SDSS2 red band image. **Left bottom:** HI spectrum. Constructed in a similar manner to UGC 1503. **Right bottom:** Velocity Field. The HI intensity weighted mean velocity (moment 1) is shown in RGB color scale and in white contours from 6150 to 6450 km s^{-1} in steps of 21 km s^{-1} . The black ellipse shows the beam size.

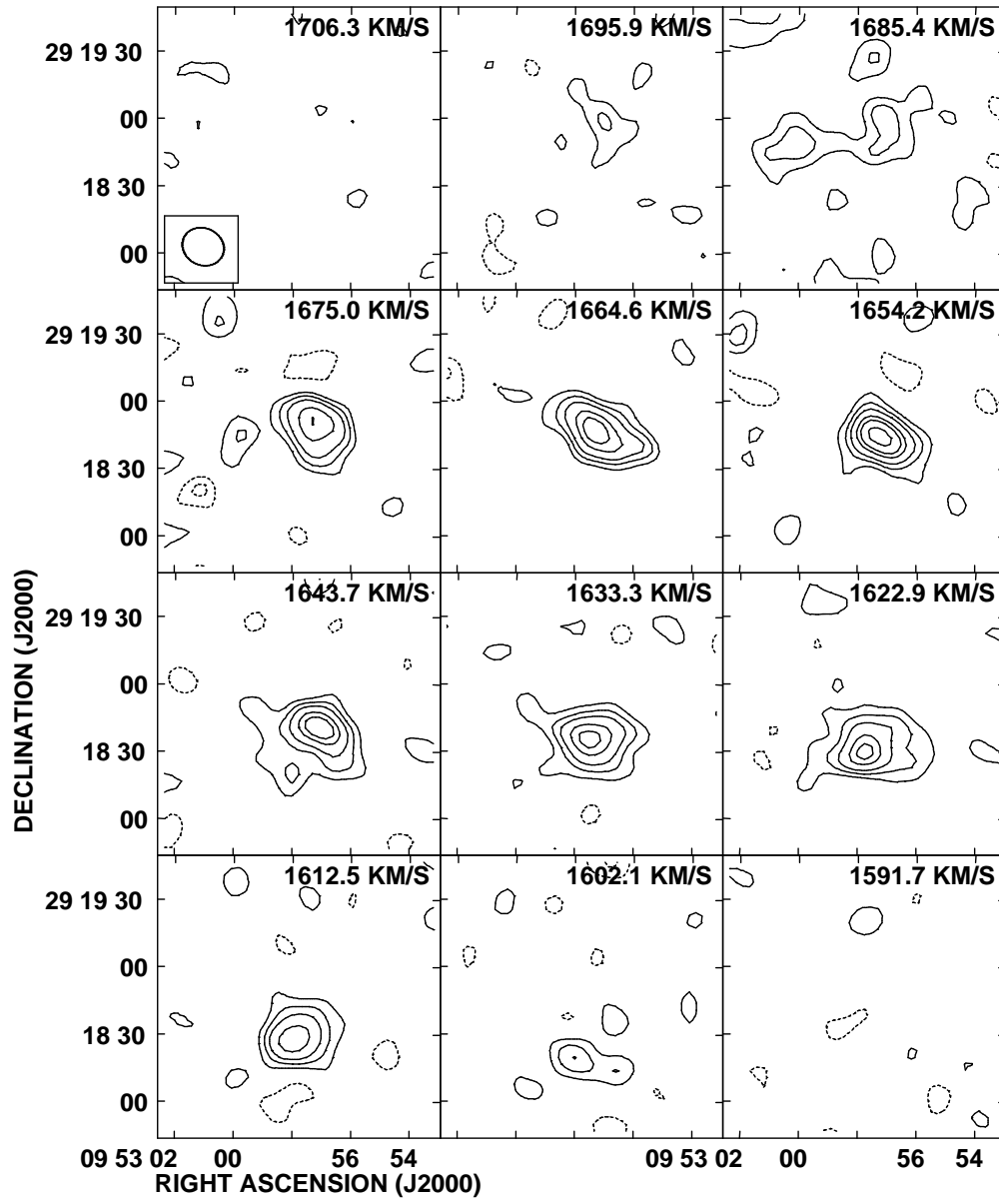


FIG. 23.— [KUG] 950+295: Individual channel maps showing HI emission. Contour levels are -5 , -3 , 3 , 5 , 12 , and 15 times $0.6 \text{ mJy beam}^{-1} \sim 1\sigma$. Negative contours are grey. The velocity of each channel (in km s^{-1}) is indicated at the top of each panel and the beam size in the first panel in the bottom left corner.

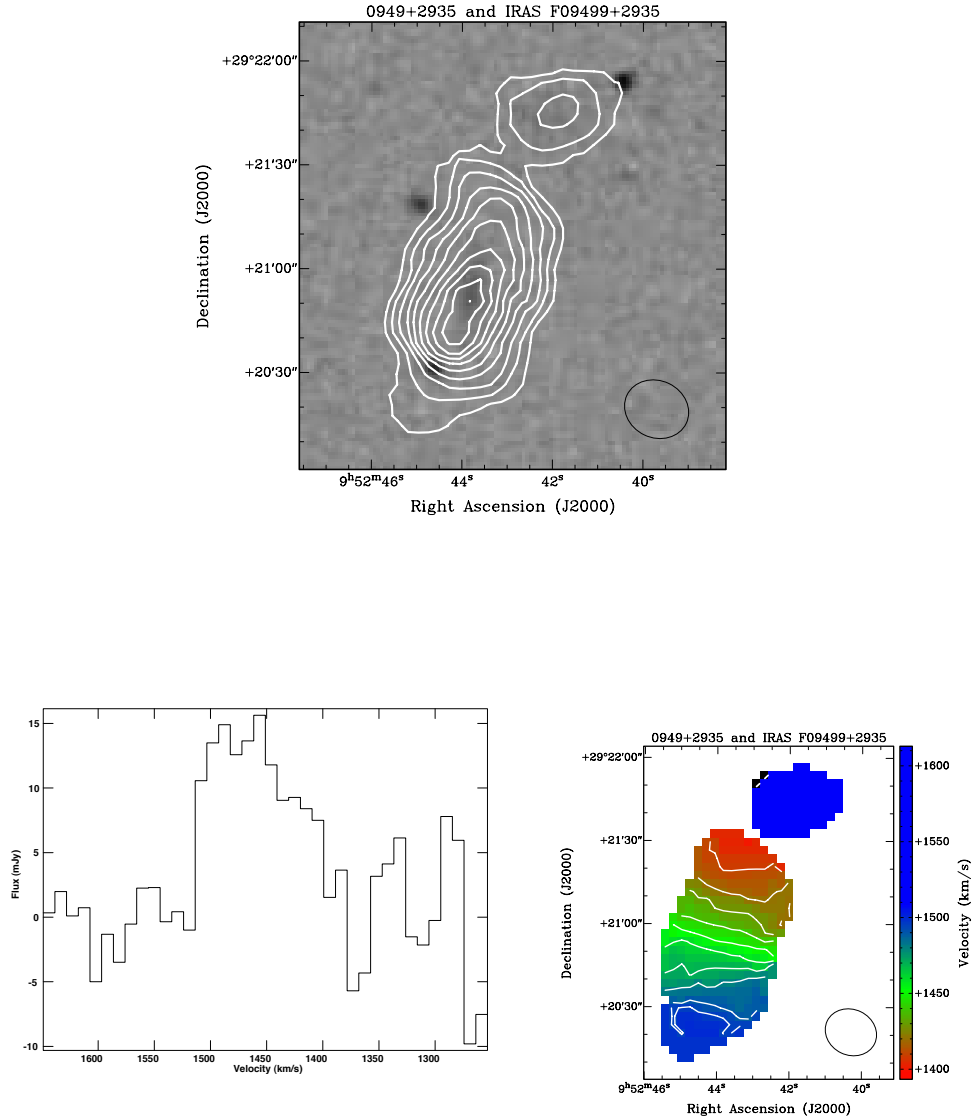


FIG. 24.— DS96 0949+2935 and an unknown source. **Top:** Solid black (positive) and solid grey (negative) contours show the HI integrated intensity in units of -20% , -10% , -1% , 1% , 10% , 20% , 30% , 40% , 50% , 60% , 70% , 80% and 90% of the peak ($0.29 \text{ Jy beam}^{-1} \text{ km s}^{-1} = 1.0 \times 10^{21} \text{ cm}^{-2}$). The grey scale image is an SDSS2 red band image. **Left bottom:** HI spectrum. Constructed in a similar manner to UGC 1503. **Right bottom:** Velocity Field. The HI intensity weighted mean velocity (moment 1) is shown in RGB color scale and in white contours from 6150 to 6450 km s^{-1} in steps of 21 km s^{-1} . The black ellipse shows the beam size.

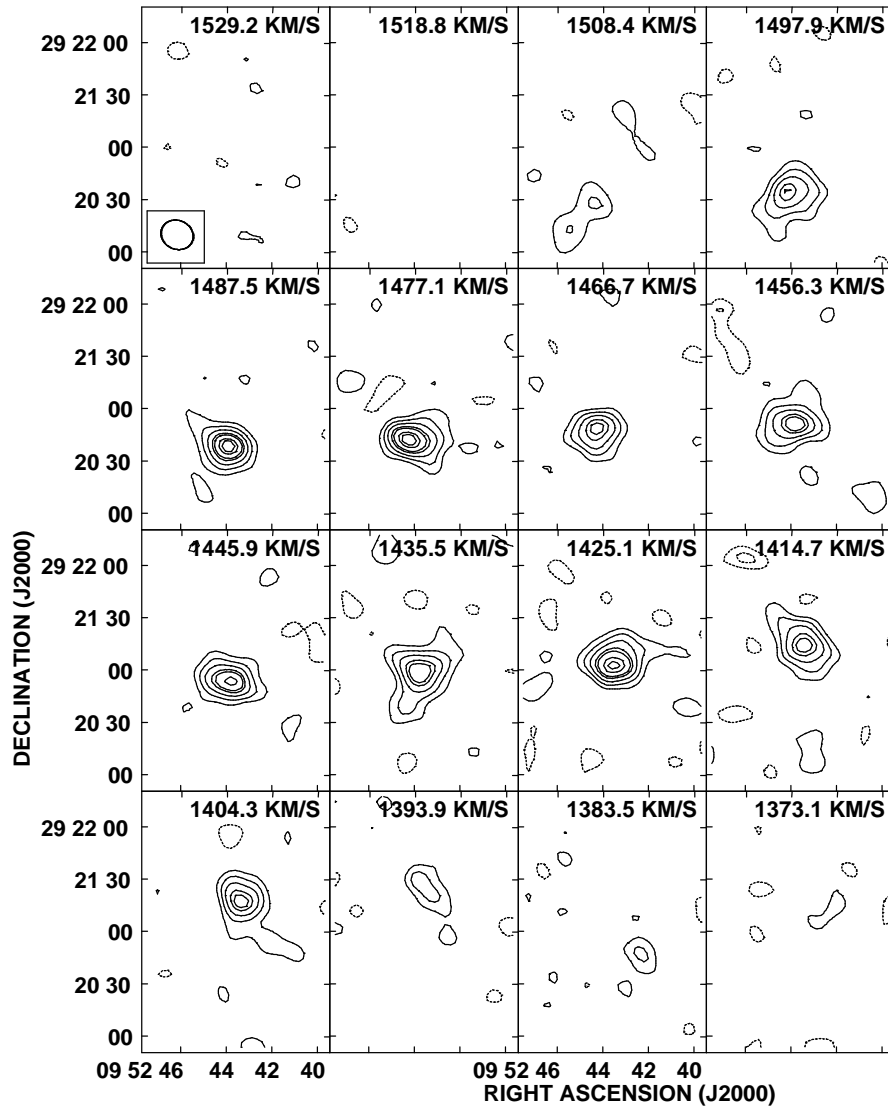


FIG. 25.— 0949+2935: Individual channel maps showing HI emission. Contour levels are -5, -3, 3, 5, 6, 6.5, 6.8, 7.2, and 7.4 times $0.6 \text{ mJy beam}^{-1} \sim 1\sigma$. Negative contours are grey. The velocity of each channel (in km s^{-1}) is indicated at the top of each panel and the beam size in the first panel in the bottom left corner.

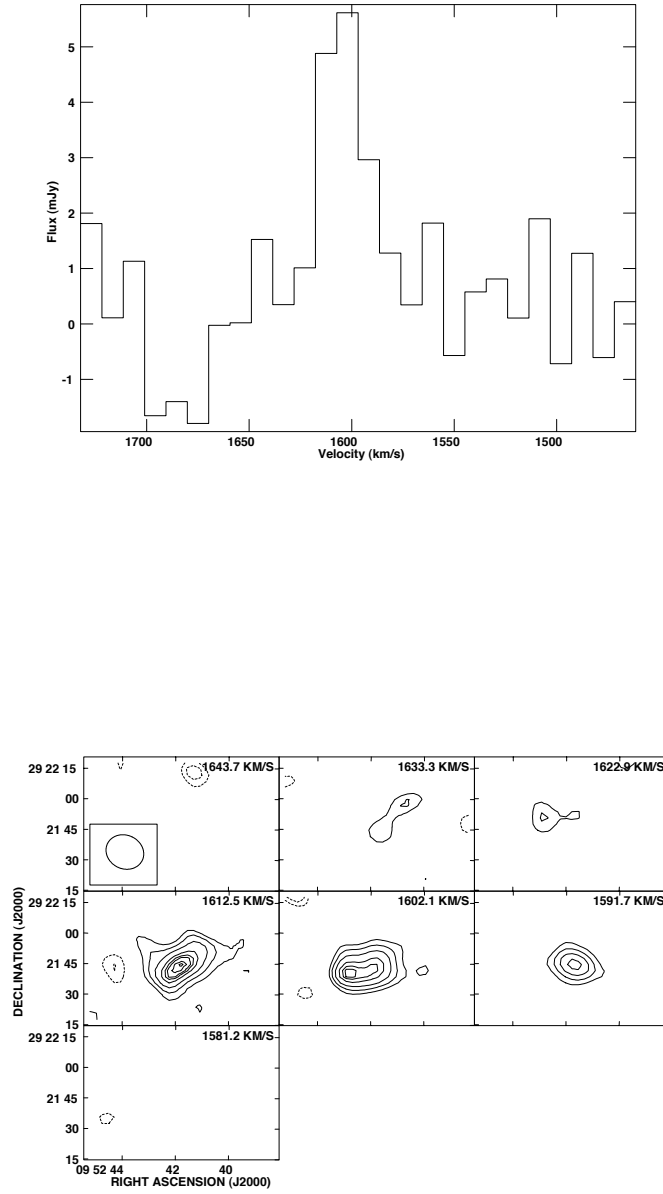


FIG. 26.— Unknown source. **Top:** HI spectrum. Constructed in a similar manner to UGC 1503. **Bottom:** Individual channel maps showing HI emission. Contour levels are $-4, -3, 3, 4, 5, 7, 9, 10, 12,$ and 13 times $0.6 \text{ mJy beam}^{-1} \sim 1\sigma$. Negative contours are grey. The velocity of each channel (in km s^{-1}) is indicated at the top of each panel and the beam size in the first panel in the bottom left corner.

REFERENCES

- Alatalo, K., Davis, T. A., Bureau, M., Young, L. M., Blitz, L., Crocker, A. F., Bayet, E., Bois, M., Bournaud, F., Cappellari, M., Davies, R. L., de Zeeuw, P. T., Duc, P.-A., Emsellem, E., Khochfar, S., Krajnović, D., Kuntschner, H., Lablanche, P.-Y., Morganti, R., McDermid, R. M., Naab, T., Oosterloo, T., Sarzi, M., Scott, N., Serra, P., & Weijmans, A.-M. 2012, ArXiv e-prints
- Atthey, A., Bregman, J., Bregman, J., Temi, P., & Sauvage, M. 2002, *ApJ*, 571, 272
- Balcells, M., van Gorkom, J. H., Sancisi, R., & del Burgo, C. 2001, *AJ*, 122, 1758
- Blitz, L., & Rosolowsky, E. 2004a, in *Astronomical Society of the Pacific Conference Series*, Vol. 323, *Star Formation in the Interstellar Medium: In Honor of David Hollenbach*, ed. D. Johnstone, F. C. Adams, D. N. C. Lin, D. A. Neufeld, & E. C. Ostriker, 89B
- Blitz, L., & Rosolowsky, E. 2004b, *ApJ*, 612, L29
- . 2006, *ApJ*, 650, 933
- Brightenti, F., & Mathews, W. G. 1997, *ApJ*, 490, 592
- Burns, J. O., Roettiger, K., Pinkney, J., Perley, R. A., Owen, F. N., & Voges, W. 1994, in *Bulletin of the American Astronomical Society*, Vol. 26, *Bulletin of the American Astronomical Society*, 1511
- Cappellari, M., Bacon, R., Bureau, M., Damen, M. C., Davies, R. L., de Zeeuw, P. T., Emsellem, E., Falcón-Barroso, J., Krajnović, D., Kuntschner, H., McDermid, R. M., Peletier, R. F., Sarzi, M., van den Bosch, R. C. E., & van de Ven, G. 2006, *MNRAS*, 366, 1126
- Cappellari, M., Emsellem, E., Bacon, R., Bureau, M., Davies, R. L., de Zeeuw, P. T., Falcón-Barroso, J., Krajnović, D., Kuntschner, H., McDermid, R. M., Peletier, R. F., Sarzi, M., van den Bosch, R. C. E., & van de Ven, G. 2007, *MNRAS*, 379, 418
- Cappellari, M., Emsellem, E., Krajnović, D., McDermid, R. M., Serra, P., Alatalo, K., Blitz, L., Bois, M., Bournaud, F., Bureau, M., Davies, R. L., Davis, T. A., de Zeeuw, P. T., Khochfar, S., Kuntschner, H., Lablanche, P.-Y., Morganti, R., Naab, T., Oosterloo, T., Sarzi, M., Scott, N., Weijmans, A.-M., & Young, L. M. 2011, *MNRAS*, 416, 1680
- Cayatte, V., van Gorkom, J. H., Balkowski, C., & Kotanyi, C. 1990, *AJ*, 100, 604
- Ciotti, L., D’Ercole, A., Pellegrini, S., & Renzini, A. 1991, *ApJ*, 376, 380
- Combes, F., Young, L. M., & Bureau, M. 2007, *MNRAS*, 377, 1795
- Condon, J. J., Cotton, W. D., Greisen, E. W., Yin, Q. F., Perley, R. A., Taylor, G. B., & Broderick, J. J. 1998, *AJ*, 115, 1693
- Cornwell, T. J., Uson, J. M., & Haddad, N. 1992, *AAP*, 258, 583
- Crocker, A. F., Bureau, M., Young, L. M., & Combes, F. 2011, *MNRAS*, 410, 1197
- Crocker, A. F., Krips, M., Young, L. M., Bureau, M., Combes, F., & Atlas3d Team. 2010, in *Bulletin of the American Astronomical Society*, Vol. 42, *Bulletin of the American Astronomical Society*, 484
- Davis, T. A., Alatalo, K., Sarzi, M., Bureau, M., Young, L. M., Blitz, L., Serra, P., Crocker, A. F., Krajnović, D., McDermid, R. M., Bois, M., Bournaud, F., Cappellari, M., Davies, R. L., Duc, P.-A., de Zeeuw, P. T., Emsellem, E., Khochfar, S., Kuntschner, H., Lablanche, P.-Y., Morganti, R., Naab, T., Oosterloo, T., Scott, N., & Weijmans, A.-M. 2011, *MNRAS*, 417, 882
- de Vaucouleurs, G. 1948, *Annales d’Astrophysique*, 11, 247
- de Vaucouleurs, G., de Vaucouleurs, A., Corwin, Jr., H. G., Buta, R. J., Paturel, G., & Fouque, P. 1991, *Third Reference Catalogue of Bright Galaxies* (Springer-Verlag Berlin Heidelberg New York)
- di Serego Alighieri, S., Gavazzi, G., Giovanardi, C., Giovanelli, R., Grossi, M., Haynes, M. P., Kent, B. R., Koopmann, R. A., Pellegrini, S., Scodreggio, M., & Trinchieri, G. 2007, *AAP*, 474, 851
- Dickey, J. M., & Lockman, F. J. 1990, *ARAA*, 28, 215
- Donzelli, C. J., & Davoust, E. 2003, *AAP*, 409, 91
- Dressel, L. L. 1987, in *Bulletin of the American Astronomical Society*, Vol. 19, *Bulletin of the American Astronomical Society*, 1032
- Duprie, K., & Schneider, S. E. 1996, *AJ*, 112, 937
- Elmegreen, B. G. 1993, *ApJ*, 411, 170
- Emsellem, E., Cappellari, M., Krajnović, D., van de Ven, G., Bacon, R., Bureau, M., Davies, R. L., de Zeeuw, P. T., Falcón-Barroso, J., Kuntschner, H., McDermid, R., Peletier, R. F., & Sarzi, M. 2007, *MNRAS*, 379, 401
- Emsellem, E., Cappellari, M., Peletier, R. F., McDermid, R. M., Bacon, R., Bureau, M., Copin, Y., Davies, R. L., Krajnović, D., Kuntschner, H., Miller, B. W., & de Zeeuw, P. T. 2004, *MNRAS*, 352, 721
- Faber, S. M., & Gallagher, J. S. 1976, *ApJ*, 204, 365
- Falco, E. E., Impey, C. D., Kochanek, C. S., Lehár, J., McLeod, B. A., Rix, H., Keeton, C. R., Muñoz, J. A., & Peng, C. Y. 1999, *ApJ*, 523, 617
- Fisher, D., Franx, M., & Illingworth, G. 1995, *ApJ*, 448, 119
- Fumagalli, M., Krumholz, M. R., & Hunt, L. K. 2010, *ApJ*, 722, 919
- Georgakakis, A., Hopkins, A. M., Caulton, A., Wiklind, T., Terlevich, A. L., & Forbes, D. A. 2001, *MNRAS*, 326, 1431
- Greisen, E. W. 2003, in *Astrophysics and Space Science Library*, Vol. 285, *Astrophysics and Space Science Library*, ed. A. Heck, 109
- Grossi, M., di Serego Alighieri, S., Giovanardi, C., Gavazzi, G., Giovanelli, R., Haynes, M. P., Kent, B. R., Pellegrini, S., Stierwalt, S., & Trinchieri, G. 2009, *AAP*, 498, 407
- Gunn, J. E., & Gott, III, J. R. 1972, *ApJ*, 176, 1
- Huchtmeier, W. K., Karachentsev, I. D., & Karachentseva, V. E. 2000, *AAPS*, 147, 187
- Huchtmeier, W. K., & Richter, O. 1986, *AAPS*, 64, 111
- Huchtmeier, W. K., Sage, L. J., & Henkel, C. 1995, *AAP*, 300, 675
- Kalberla, P. M. W., Burton, W. B., Hartmann, D., Arnal, E. M., Bajaja, E., Morras, R., & Pöppel, W. G. L. 2005, *AAP*, 440, 775
- Karachentsev, I. D., Sharina, M. E., Dolphin, A. E., Grebel, E. K., Geisler, D., Guhathakurta, P., Hodge, P. W., Karachentseva, V. E., Sarajedini, A., & Seitzer, P. 2003, *AAP*, 398, 467
- Krumholz, M. R., McKee, C. F., & Tumlinson, J. 2008, *ApJ*, 689, 865
- . 2009, *ApJ*, 693, 216
- Lake, G., Schommer, R. A., & van Gorkom, J. H. 1987, *ApJ*, 314, 57
- Leroy, A. K., Walter, F., Brinks, E., Bigiel, F., de Blok, W. J. G., Madore, B., & Thornley, M. D. 2008, *AJ*, 136, 2782
- Lucero, D. M., Young, L. M., & van Gorkom, J. H. 2005, *AJ*, 129, 647
- McDermid, R. M., Bacon, R., Kuntschner, H., Emsellem, E., Shapiro, K. L., Bureau, M., Cappellari, M., Davies, R. L., Falcón-Barroso, J., Krajnović, D., Peletier, R. F., Sarzi, M., & de Zeeuw, P. T. 2006, *New Astronomy Review*, 49, 521
- McKee, C. F., & Krumholz, M. R. 2010, *ApJ*, 709, 308
- Morganti, R., de Zeeuw, P. T., Oosterloo, T. A., McDermid, R. M., Krajnović, D., Cappellari, M., Kenn, F., Weijmans, A., & Sarzi, M. 2006, *MNRAS*, 371, 157
- Nakanishi, H., Kuno, N., Sofue, Y., Sato, N., Nakai, N., Shioya, Y., Tosaki, T., Onodera, S., Sorai, K., Egusa, F., & Hirota, A. 2006, *ApJ*, 651, 804
- Nakazawa, K., Kawano, N., Fukazawa, Y., Egawa, C., Kitaguchi, T., Kawaharada, M., Makishima, K., Ota, N., Tokoi, K., Sato, K., Ishisaki, Y., Ohashi, T., Yamasaki, N., & Suzaku Team. 2007, *Progress of Theoretical Physics Supplement*, 169, 45
- Nulsen, P. E. J. 1982, *MNRAS*, 198, 1007
- Oosterloo, T. A., Morganti, R., Sadler, E. M., van der Hulst, T., & Serra, P. 2007, *AAP*, 465, 787
- O’Sullivan, E., Forbes, D. A., & Ponman, T. J. 2001, *MNRAS*, 328, 461
- Roberts, M. S., & Haynes, M. P. 1994, *ARAA*, 32, 115
- Rothberg, B., & Joseph, R. D. 2006, *AJ*, 132, 976
- Sadler, E. M., Oosterloo, T. A., Morganti, R., & Karakas, A. 2000, *AJ*, 119, 1180
- Sage, L. J., & Welch, G. A. 2006, *ApJ*, 644, 850
- Sage, L. J., Welch, G. A., & Young, L. M. 2007, *ApJ*, 657, 232

- Serra, P., Oosterloo, T., Morganti, R., Alatalo, K., Blitz, L., Bois, M., Bournaud, F., Bureau, M., Cappellari, M., Crocker, A. F., Davies, R. L., Davis, T. A., de Zeeuw, P. T., Duc, P.-A., Emsellem, E., Khochfar, S., Krajnović, D., Kuntschner, H., Lablanche, P.-Y., McDermid, R. M., Naab, T., Sarzi, M., Scott, N., Trager, S. C., Weijmans, A.-M., & Young, L. M. 2012, *MNRAS*, 422, 1835
- Skrutskie, M. F., Cutri, R. M., Stiening, R., Weinberg, M. D., Schneider, S., Carpenter, J. M., Beichman, C., Capps, R., Chester, T., Elias, J., Huchra, J., Liebert, J., Lonsdale, C., Monet, D. G., Price, S., Seitzer, P., Jarrett, T., Kirkpatrick, J. D., Gizis, J. E., Howard, E., Evans, T., Fowler, J., Fullmer, L., Hurt, R., Light, R., Kopan, E. L., Marsh, K. A., McCallon, H. L., Tam, R., Van Dyk, S., & Wheelock, S. 2006, *AJ*, 131, 1163
- Smith, R. J., Lucey, J. R., Hudson, M. J., Schlegel, D. J., & Davies, R. L. 2000, *MNRAS*, 313, 469
- Theureau, G., Bottinelli, L., Coudreau-Durand, N., Gouguenheim, L., Hallet, N., Loulergue, M., Paturel, G., & Teerikorpi, P. 1998, *AAPS*, 130, 333
- van Driel, W., & van Woerden, H. 1991, *AAP*, 243, 71
- Wegner, G., Bernardi, M., Willmer, C. N. A., da Costa, L. N., Alonso, M. V., Pellegrini, P. S., Maia, M. A. G., Chaves, O. L., & Rit e, C. 2003, *AJ*, 126, 2268
- Welch, G. A., & Sage, L. J. 2003, *ApJ*, 584, 260
- Welch, G. A., Sage, L. J., & Young, L. M. 2010, *ApJ*, 725, 100
- Wiklund, T., Combes, F., & Henkel, C. 1995, *AAP*, 297, 643
- Young, L. M. 2002, *AJ*, 124, 788
- . 2005, *ApJ*, 634, 258
- Young, L. M., Bendo, G. J., & Lucero, D. M. 2009, *AJ*, 137, 3053
- Young, L. M., Bureau, M., & Cappellari, M. 2008, *ApJ*, 676, 317
- Young, L. M., Bureau, M., Davis, T. A., Combes, F., McDermid, R. M., Alatalo, K., Blitz, L., Bois, M., Bournaud, F., Cappellari, M., Davies, R. L., de Zeeuw, P. T., Emsellem, E., Khochfar, S., Krajnović, D., Kuntschner, H., Lablanche, P.-Y., Morganti, R., Naab, T., Oosterloo, T., Sarzi, M., Scott, N., Serra, P., & Weijmans, A.-M. 2011, *MNRAS*, 414, 940